

DEVELOPMENT OF A CFD SIMULATION FRAMEWORK FOR
AEROTHERMAL ANALYSES OF ELECTRIC VEHICLE BATTERY PACKS

by

Ayushi Jain

A thesis submitted to the faculty of
The University of North Carolina at Charlotte
in partial fulfillment of the requirements
for the degree of Master of Science in
Mechanical Engineering

Charlotte

2021

Approved by:

Dr. Mesbah Uddin

Dr. Jun Xu

Dr. Amirhossein Ghasemi

ABSTRACT

AYUSHI JAIN. Development of a CFD Simulation Framework for Aerothermal Analyses of Electric Vehicle Battery Packs. (Under the direction of DR. MESBAH UDDIN)

Lithium-ion batteries (LIB) are widely being used in the field of electric vehicles, their high-power density, low resistance, compactness and low self-discharge rate. These make LIBs an ideal choice for use in electric vehicles (EV). To increase the reliability of LIBs, a proper battery thermal management system is required. This thesis presents a finite volume based Computational Fluid Dynamics (CFD) aero-thermal analysis for a pack of high energy density cylindrical lithium-ion batteries. This study presents first the development of a CFD framework required for a comprehensive aero-thermal investigation. This includes investigations on the effectiveness of turbulence modeling approaches in capturing local hot-spots developed for a range of inlet velocities and configurations of the lithium-ion battery pack. Turbulence models investigated include Mentors SST $k - \omega$, Launder and Spalding standard $k - \epsilon$, realizable $k - \epsilon$ and elliptic blending $k - \epsilon$. The results from these simulations are compared against published experimental wind-tunnel data. Simcenter Battery Design Studio (BDS) is used to generate a detailed and in-dept model of the LG INR 18650 MJ1 (LiNiCoMnO₂) cell. The cell from BDS is imported in Simcenter Starccm+ 2020.2 where the simulation is set-up to monitor voltage variation, discharge rate current, temperature distribution within the pack, maximum temperature of aligned, staggered, and cross configuration for various inlet velocities. The results of these simulations are compared, and it is found that, in spite of all its short comings, the standard $k - \epsilon$ model is the most accurate model for such analysis. It is also observed that the dependency of heat generation on discharge current is significant, the battery performance is affected by the ambient temperature, and the aligned arrangement has the best temperature uniformity and cooling effectiveness. Lastly, there is significant

effect on the stability of the simulation depending on the way the boundary condition is modeled is projected

DEDICATION

I would like to dedicate this thesis to my mother and father.

Thank you for everything.

ACKNOWLEDGEMENTS

This thesis is a work of two years during which several people were involved, and now I have an opportunity to express my gratitude toward all of them.

Firstly, I would like to thank my advisor Dr. Mesbah Uddin, who has always been supportive and has given insightful suggestions throughout this project. His advice and criticism has played a vital role in helped me grow, and has helped steer this research. I would also like to thank my committee members Dr. Jun Xu and Dr. Amir Ghassemi, there valuable guidance and support help me complete my thesis successfully.

Secondly, I would like to thank Adit Misar, for being an honest critique about my work and guiding me towards the right resources whenever I was stuck on a problem. I would also like to thank all my laboratory mates and friends Mahfuja A khudha, Shadab Sheikh, Hamed Ahani, Vincent Lee, Usman Zafar, and Harish Nair for always being there, ready to help and guide me throughout the project, for motivating me, and lifting my spirits during difficult times. This project would be much more difficult if I did not have friends/colleagues like you guys.

I would like to acknowledge the Department of Mechanical Engineering and the UNCC's High Performance Computing group for their support during the whole project. Lastly I would like to thank the Tracy Beaugard who is always present to help in regarding all the administrative work.

TABLE OF CONTENTS

LIST OF TABLES	ix
LIST OF FIGURES	x
CHAPTER 1: INTRODUCTION	1
1.1. Motivation	3
1.2. Objectives	4
1.3. Thesis Outline	5
CHAPTER 2: LITERATURE REVIEW	7
2.1. Battery Modelling	8
2.1.1. Distributed Model	9
2.1.2. The Newman Tiedemann Gu (NTG) Model	12
2.1.3. RCR Model	14
2.2. CFD Modelling	16
2.2.1. Standard $k-\epsilon$ and realizable $k-\epsilon$ model	18
2.2.2. SST $k-\omega$ model	20
2.2.3. Elliptic Blending model	22
CHAPTER 3: NUMERICAL SETUP	25
3.1. Battery set-up	25
3.2. 2D Analysis	29
3.3. 3D Analysis	32
CHAPTER 4: RESULTS AND DISCUSSION	37
4.1. Aligned arrangement	38

	viii
4.2. Staggered	43
4.3. Cross	44
4.4. Aligned, Staggered, and Cross arrangement	46
CHAPTER 5: CONCLUSIONS	51
REFERENCES	54

LIST OF TABLES

TABLE 3.1: Battery specification [1]	26
TABLE 3.2: Parameterization of NMC-811/SiC electrodes [2]	27
TABLE 3.3: Battery pack design parameters [1]	27
TABLE 3.4: Mesh independence study	33
TABLE 3.5: Time-step independence study	36

LIST OF FIGURES

FIGURE 2.1: NTG Model schematic diagram	12
FIGURE 2.2: RCR Model	15
FIGURE 3.1: Aligned geometry	28
FIGURE 3.2: Staggered geometry	28
FIGURE 3.3: Cross geometry	28
FIGURE 3.4: 2D steady state simulation set-up	29
FIGURE 3.5: Mesh scene for 2D set-up	30
FIGURE 3.6: Velocity plot for 2D set-up	30
FIGURE 3.7: Total pressure coefficient for 2D set-up	31
FIGURE 3.8: Layout	32
FIGURE 3.9: Volume controls	34
FIGURE 3.10: Wake refinement	34
FIGURE 3.11: Prism Layers development around the battery	35
FIGURE 4.1: Turbulence models effectiveness comparison	39
FIGURE 4.2: Aligned arrangement - temperature scene, inlet $V = 2$ m/s	40
FIGURE 4.3: Inlet velocity effect on heat dissipation study	41
FIGURE 4.4: 1C discharge rate results	42
FIGURE 4.5: Staggered temperature scene, inlet $V = 2$ m/s	43
FIGURE 4.6: Staggered arrangement plots	44
FIGURE 4.7: Cross arrangement plots	45
FIGURE 4.8: Cross arrangement temperature distribution, $V = 2$ m/s	46

FIGURE 4.9: Arrangement comparison - maximum temperature, inlet $V = 2$ m/s	46
FIGURE 4.10: Arrangement comparison - maximum temperature rise, inlet $V = 2$ m/s	47
FIGURE 4.11: Aligned velocity scene, inlet $V = 2$ m/s	47
FIGURE 4.12: Aligned velocity scene, inlet $V = 2$ m/s	48
FIGURE 4.13: Staggered velocity scene, inlet $V = 2$ m/s	48
FIGURE 4.14: Staggered velocity scene, inlet $V = 2$ m/s	49
FIGURE 4.15: Cross velocity scene, inlet $V = 2$ m/s	50
FIGURE 4.16: Cross velocity scene, inlet $V = 2$ m/s	50

CHAPTER 1: INTRODUCTION

With the advancement in electric vehicles (EV), it has been established that the power battery plays a significant role in the performance of the vehicle. Lithium-ion batteries (LIB) are widely used in this field because of the high power density, high voltage, compactness, low resistance and low self-discharge rate. It also has an added advantage of stable performance, long-life cycle and less carbon footprints. However, the major drawback are the frequently reported fire or explosion accidents [3], because of improper battery thermal management system (BTMS).

The operating temperature of the LIB highly affects the reliability and durability of the battery, extreme operating temperatures both high and low, can cause increase in rate of degradation, and shorten the lifespan. The allowable discharge temperature range is from -20° to 60° C. The optimum battery operating temperature is considered to be 20° to 40° C [4], a maximum temperature difference of 5° among the batteries in the pack is desirable. The cells energy storage and cycle life can reduce significantly when the cell is operated at a temperature below 0° or above 40° C.

The growth of solid electrolyte interface layer is promoted at high temperatures, which reduces the power delivery by increasing the internal resistance. At extreme conditions, the separator may melt causing an internal short circuit, this can lead to uncontrollable rise in temperature (thermal runaway). Depending on the battery chemistry the energy and gases released during this process, can cause an explosion. Contrarily, if the operating temperature is below 0° C, it leads to formation of metallic lithium around the anode during charging. This deposition can cause malfunction during recharging of the batteries over time.

For proper functioning at all temperatures, battery packs are tested experimen-

tally and computationally, before releasing it in the market. There is a considerable amount of work done in studying the effect of strain rate and solvent behaviors of separators in Lithium Ion [5], [6], penetration induced thermal runaway [7], thermal abuse tolerance, etc. computationally. There has been a considerable amount of experimental work as well [8], [9], [10].

As the conditions for which the battery thermal management system is investigated both experimentally and numerically are limited, an extensive research on this issue with a combination of various battery geometry, configuration and physical properties like different state of charge of the cell, battery cell arrangement will have a wide ranging importance in the industry. Conducting these tests experimentally following all the safety and environment regulations is an expensive, tedious and time consuming process. This can be prevented by conducting simulations computationally, here the role of computational fluid dynamics comes into consideration. There have been some of the previously reported numerical works which shows results with some degree of correlation with experiment, still significant discrepancies remain between the experiment and CFD results. Most of the previously reported numerical models [5], [6], [7] are based off the finite element method (FEM). The proposed research work uses a finite volume method (FVM) as it is the most widely used aero-thermal analysis tool as used by the automotive OEMs.

With the accessibility of high-speed performing computers, turbulence modeling has secured a place of effective problem solver in engineering applications. This thesis focuses on a coupled aero-thermal analysis, studying the heat generation within the battery and heat dissipation in the fluid domain. The models used in this study are

- Launder and Spalding $k-\epsilon$ [11],
- Mentors $k-\omega$ SST [12],
- Realizable $k-\epsilon$ [13], and

- Elliptic blending $k-\epsilon$ [14]

1.1 Motivation

With the increasing global warming and the awareness of the need to protect the environment, the application of different forms of energy are being highly valued worldwide. The new technology comes with its own set of challenges, it should be safe and robust. Lithium ion batteries is becoming one of the most widely used technology for powering electrical vehicles. Studies are being conducted to monitor the working of lithium-ion batteries in extreme conditions [15], [6], [9]. Battery thermal management investigation can be a hazardous process, while conducting these experiments one must follow strict environmental regulations and guidelines.

Conducting the experiments considering all environment regulations can become an expensive, time consuming and tedious process. The existing works focuses on finite element method in analyzing the structural strength, mechanical integrity [16], failure and fracture of the shell, torsion test [17] etc. There is research conducted in the area of finite volume based methods as well, in these models the battery heat generation is modelled in form of a resistance network and homogeneous properties are assumed throughout the cell [18], [19], for a majority of cases.

The finite volume method is a widely used numerical tool in the automotive OEMs. The CFD analysis that involves a battery modelled using an advanced battery modeling tool provides a base for an electrical vehicle aero-thermal simulations. Battery design studio provides a platform for detail modelling of the battery while considering parameters as anode material, cathode material, particle radius, separator, internal tabs etc. A coupled simulation that involves BDS and Simcenter Starccm+ which is a very popular tool for finite volume method based numerical analysis in the automotive industry is designed. This thesis aims at providing a framework for battery pack aero-thermal analysis which can be further coupled with the full automotive body, and simulated together all on one platform.

1.2 Objectives

Modern era is swiftly moving towards a more environment conscious world, with that there is development of pure battery vehicles (BEV), hybrid electric vehicle (HEV) and plug-in hybrid electric vehicles (PHEV). The crux of electric vehicle development narrows down to battery performance, the objective being improvising the efficiency, safety, and robustness of batteries. Battery thermal management system plays a pivotal role in ensuring this, and is responsible for maintaining the heat distribution within the battery pack.

In order to achieve optimum efficiency within the battery pack, governing and regulating the temperature distribution, heat production, and heat dissipation play a detrimental role. To investigate this, numerical aero-thermal analyses involving different turbulence models and a detailed battery model are studied. The battery is developed using Battery Design Studio and the aero-thermal analyses are conducted on Simcenter StarCCM+ as it is a versatile tool well known in the automotive industry.

This study includes the effects of changing inlet velocity on temperature distribution and heat dissipation, change in heat generation with varying discharge rates, and determining the optimum battery pack arrangement with respect to temperature uniformity and cooling effectiveness. The results are validated with available experimental data to determine the most appropriate numerical method. This thesis aims to establish a framework for aero-thermal analyses of battery packs for future studies.

To summarize, the objectives of this study are:

- develop a framework of CFD simulation methodologies for aero-thermal analyses of lithium-ion battery packs using a finite volume commercial CFD code,
- investigate the efficacy of various commonly used turbulence models in predicting the maximum temperature rise and temperature difference within a LIB

battery pack,

- examine the effects of changes in inlet velocity on temperature variation with the the pack in order to predict the ideal velocity for the best battery performance and efficiency,
- analyze the effects of varying discharge rates on heat generation which ultimately affects the temperature rise, and
- investigate the impacts of aligned, cross and staggered cell arrangements within the pack on the aero-thermal flow-fields within the pack, and determine the preferred battery pack arrangement by evaluating the cooling effectiveness and temperature uniformity.

1.3 Thesis Outline

The thesis is organized in the following manner:

- Chapter 2 discusses the background of battery designing and development, major problems faced in battery usage, all previous relevant work has been compiled. It also details about turbulence modeling and its significance in designing of battery thermal management system, the turbulence models considered for this study are discussed.
- Chapter 3 provides information about the numerical modelling of the battery and the coupled simulation details, the development of the battery, used for analysis.
- Chapter 4 includes the battery parameters, simulation setup, the importance of external casing geometry, meshing strategy, and other details regarding the setup.

- Chapter 5 contains the results and conclusions from the investigations on the prediction capabilities of turbulence models in a simulation involving multiple bodies.
- Chapter 7 concludes the thesis with a summary and outlines scope for future analysis of the work.

CHAPTER 2: LITERATURE REVIEW

Electric vehicles are becoming more reliable and environment friendly alternative to internal combustion engines. Companies like Tesla, Rivian, Lucid-Motors, Zoox which specialize in sole electric vehicle are introducing faster, more reliable vehicles, breaking down every barrier against electric vehicles. The traditional automotive companies are also inclining towards having an electric vehicle (EV), battery electric vehicle (BEV), hybrid electric vehicle (HEV) or plug-in hybrid electric vehicle (PHEV) line. With this development the focus on the battery pack has increased, every aspect starting from chemical composition [20] to heat generation and dissipation is studied in detail.

The biggest constrain observed in battery designing is the influence of temperature on battery performance [21]. The batteries can ignite, rupture or even explode at elevated temperature, thermal runaway and high degradation are also observed at high temperature. Therefore it is essential to have a well designed battery thermal management system (BTMS). It limits the temperature variation within the pack and maintains a uniform temperature distribution. The battery thermal management system investigates the following :

- The effect of fluid, utilized for forced cooling, air cooling [22]. liquid cooling [21], heat pipe cooling [23] and phase change material cooling [24]
- Natural cooling system and forced cooling system, based on whether the system has a cooling fan [24]
- Passive cooling or active cooling, depending on how the inlet is cooled
- Inlet air velocity and temperature [3]

- Cooling structure of the battery pack, modeling the inlet shape [25], layout of the batteries within the pack [26], etc

There have been several experimental and CFD analysis of the battery thermal management system [27], [19], in which the heat generated by the battery has been simplified and several influencing factors have been neglected while modelling the heat generation. CFD analysis where they consider the maximum heat generated by the battery and model it as a constant heat value [18] to give us an estimate of the temperature of the system. Other researches involve treating the battery as a resistance [19], in a circuit and modelling the heat generation accordingly, while these assumptions gives us an overview of the heat generation within a battery pack a more detailed battery will help constructing a more realistic simulation. In this thesis, we attempt to provide a detail method of battery modelling using battery design studio and its aero-thermal analysis, testing a range of turbulence models, comparing the results at different rate of discharge, inlet velocity and inlet temperature.

2.1 Battery Modelling

Traditionally battery designing and testing involved manufacturing of a cell with desired chemical and physical properties and then testing it to see if it meets the criteria. Numerical battery modeling is the numerical generation of the thermal and electrical response of the battery over path of a load cycle. In this study the batteries are designed using Simcenter Battery Design Studio (BDS), it is a platform which combines the electro-chemical properties of electrolyte and electrode material, and accurately models their representation. By using BDS we can design the battery with the desired specifications. The software is designed for battery development, we are able to generate a battery cell file considering all the cell parameters, the software accounts for all the parts of the battery such as the jelly roll, mandrel, tab-connectors, separators, etc. Conducting a study which involves detailed battery heat generation and turbulence modelling, to study the heat dissipation of the battery pack can be

highly useful for electric-vehicle thermal management system development.

BDS has the ability to captures important attributes of a cell such as open circuit voltage, nominal capacity, electrode dimensions, etc. This tool focuses on lithium-ion chemistry and gives us the freedom to define aspects of construction of the electrochemical cell. Cell designers can reduce the cost of building prototype and optimizing design by using this tool and creating a battery cell virtually.

The IET (current(I), Voltage (E), Temperature(T)) is responsible for the electronic and thermal configuration of the battery. BDS provides three IET model for 3D analysis of battery. The next section describes the three models in detail.

2.1.1 Distributed Model

The distributed(DIST) model is from the DUAL model family, it is a recently developed model in battery design studio. The Distributed NP and Distributed 3D models account for multiple particles, current distribution along and cross the current collectors as well as across the cell. A galvanostatic charge discharge of the anode-separator-cathode (cell sandwich) is modeled. A one-dimension transport of the lithium ion is considered from the negative electrode to separator to positive electrode. The theory of this model is derived from the work of Newman and Doyle et al [28]

The model equations are:

Liquid-phase mass balance: [29]

$$\epsilon \frac{\partial c}{\partial t} = \frac{\partial}{\partial x} \left(\frac{\epsilon D \partial c}{\tau \partial x} \right) - \frac{1}{F} \frac{\partial i_{2,x}}{\partial x} \frac{\partial t_+^0}{\partial x} + (1 - t_+^0) a j_n, D = D_0 \left(1 - \frac{\partial \ln c_0}{\partial \ln c} \right) \quad (2.1)$$

Where,

ϵ = Porosity

c = Liquid-phase salt concentration, mol/m³

D = Salt diffusion coefficient, m²/s

τ = Tortuosity

F = Faraday constant, Coulombs/equivalent

i_{2x} = liquid-phase current density, A/m²

t_+^0 = transport number for lithium

a = Surface to volume ratio of active material, m²/m³

c_0 = Solvent concentration, mol/m³

Solid-phase Ohm's law: [29]

$$\frac{\partial}{\partial x} \left(\sigma \frac{\partial \phi_1}{\partial x} \right) = Faj + ai_{cap} \quad (2.2)$$

Where,

ϕ_1 = Solid-phase potential

σ = Solid-phase electronic conductivity, S/m

i_{cap} = Capacitive current density, A/m²

F = Faraday constant, Coulombs/equivalent

Liquid-phase Ohm's law: [29]

$$i_{2x} = -\frac{\kappa \epsilon \partial \phi_2}{\tau \partial x} + \frac{2\kappa \epsilon RT}{F\tau} \left(1 + \frac{\partial \ln f_A}{\partial \ln c} \right) (1 - t_+^0) \frac{\partial \ln c}{\partial x} \quad (2.3)$$

i_{2x} = Liquid-phase current density, A/m²

κ = Electrolyte conductivity, S/m

f_A = Activity coefficient, m³/mol

t_+^0 = transport number for lithium

τ = Tortuosity

Kirchoff's law: [29]

$$\frac{\partial i_{2,x}}{\partial x} = Faj + ai_{cap} \quad (2.4)$$

i_{2x} = Liquid-phase current density, A/m²

i_{cap} = Capacitive current density, A/m²

Solid-phase mass balance: [29]

$$\frac{\partial c_s}{\partial t} = \frac{-1}{r^2} \frac{\partial(r^2 N)}{\partial r}, N = -\tilde{D}_s \frac{\partial c_s}{\partial r} \quad (2.5)$$

r = radius

c_s = Solid-phase Li concentration, mol/m³

Butler-Volmer: [29]

$$j_{n,i} \cdot F = i_{0,i} \left(\frac{c_{l,s}}{c_{l,ref}} \right)^a \left(1 - \frac{c_{s,i}}{c_{s,max,i}} \right)^b \left[\exp \left(\frac{\alpha_a F \eta_i}{RT} \right) - \exp \left(\frac{-\alpha_c F \eta_i}{RT} \right) \right] \quad (2.6)$$

$$\eta_i = \phi_1 - \phi_2 - U_{eq,i} - j_{n,i} F R_{sei,i} \quad (2.7)$$

$$i_{cap} = -C \frac{d(\phi_1 - \phi_2)}{dt} \quad (2.8)$$

j_n = Local flux at active material surface, mol/(s·m²)

η = Over-potential, Volts

α_a = Anodic transfer coefficient

α_c = Cathodic transfer coefficient

ϕ_1 = Solid-phase potential, Volts

ϕ_2 = Liquid-phase potential, Volts

C = double layer capacitance, Farads/m²

The model used superposition (the ability to present at multiple states at the same time) to simulate the insertion of lithium-ion in and out of the active electrode material, it greatly simplifies the numerical calculations.

The driving force behind the mass transfer in the battery is the gradient in electrochemical potential. The equations 2.1 corresponds to this mass-transfer. The variation in potential is calculated by the current density equation (2.2, 2.3, 2.4). The butler volmer equation is used for calculating the capacitive current density from

the potential difference between solid and liquid phase. The Crank-Nicolson implicit method is used for evaluating the time derivatives.

The numerical methods is designed based on the rocking chair [30] analogy studies the shuttling of the lithium-ions oscillating between two insertion compounds.

2.1.2 The Newman Tiedemann Gu (NTG) Model

The NTG model [31] [32] [33], was developed to numerically model the constant discharge and charge behaviour of the battery. This model has proven successful for simulating large cell electro-thermal behaviour based on data gained from small cell empirical tests. Mathematical models play an important role during scaling a large-scale battery from a small scale battery as one can conduct limitless design iterations. In the NTG model the battery is considered as a voltage source connected in series with a resistor, as shown in the picture below. [29]

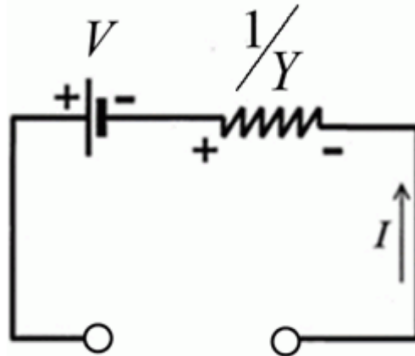


Figure 2.1: NTG Model schematic diagram

Note: Figure taken from Battery Design Studio manual guide [29]

In battery design studio, NTGP (Newman Tiedemann Gu Peukert) Table model is supported. It predicts the temperature and potential of the battery by using a constant current density value along the electrodes. This model also accounts for the current variation along the breath and height of the cell electrodes and the heat generation within the current collectors. Which makes it convenient for simulating charge-discharge behaviour of large-scale cells.

The equations of the NTG model are as follows: [29]

$$V_{cell} = V(SOC_i, T) - \frac{i}{Y(SOC_i, T)} \quad (2.9)$$

V_{cell} = Working cell voltage

SOC = state of charge

Y = Admittance term, Ohm⁻¹ m⁻²

T = Temperature, K

Discharge [29]

$$SOC_i = 1 - (1 - SOC) \frac{C_{Ah-m^{-2},0}}{C_{Ah-m^{-2},i}} \quad (2.10)$$

$C_{Ah-m^{-2},0}$ = Nominal cell capacity, Ah-m⁻²

$C_{Ah-m^{-2},i}$ = Cell capacity at current density i , Ah-m⁻²

Charge [29]

$$SOC_i = SOC \frac{C_{Ah-m^{-2},0}}{C_{Ah-m^{-2},i}} \quad (2.11)$$

$$SOC = \frac{\int i dt}{C_{Ah-m^{-2},0}} i = \frac{I}{A} \quad (2.12)$$

Where,

i = current density, A-m⁻²

I = Current, A

$$Q = I.(U_{oc} - V_{cell} - T \frac{dU}{dT}) \quad (2.13)$$

Where,

Q = Electro-chemical heat generation, W

U_{oc} = Equilibrium voltage, V

V_{cell} = Working cell voltage

From experiments which conduct constant current charge-discharge cycles at dif-

ferent rates, the parameters required for the NTG model can be obtained. The values of V (voltage term) and Y (admittance term) can be obtained from a plot of voltage vs current density at a fixed depth of discharge. V is the intercept with the voltage axis, and the Y is inverse of the slope. This approach lets us form a table of V and Y parameters as a function of discharge depth.

In Simcenter Battery Design Studio, the table values of V vs Y can be fitted to a Bezier spline, which provides a far better representation than any possible with a polynomial. Using this model BDS uses linear interpolation estimating values of the intermediate temperatures.

The NTGPTable model, lets us specify data sets corresponding to charging and discharging specifically or both charging and discharging. This model also accounts for the Peukert effect [34] i.e loss of battery capacity at higher discharge rates. These emphasis on details, make the NTGPTable model a favourable choice for simulating the electrothermal behavior of batteries during charge and discharge numerical simulation.

2.1.3 RCR Model

It was developed to provide accurate information of the State of Charge on electric vehicle batteries. The RCR model is an equivalent circuit model of the current-voltage relationship [35], [36]. This model allows you to specify temperature for a given parameter set. In RCR model all the parameters are dependent on the SOC value. The figure below represents the schematic diagram of the RCR model [29].

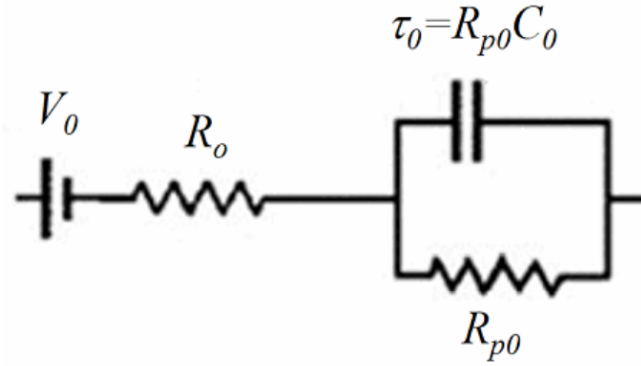


Figure 2.2: RCR Model

Note: Figure taken from Battery Design Studio manual guide [29]

RCR model equations are as follows: [29]

$$V_L = V_O - I - \frac{I}{C} \Delta T + (V_L - V_O + I \cdot R_O)_{t-\Delta t} \exp\left[\frac{-\Delta t}{\tau}\right] \quad (2.14)$$

Where,

V_o = Zero current or open circuit voltage, V

V_L = Computed cell working voltage, V

R_o = Series resistance, ohm

R_p = polarization resistance, ohm

τ = Time constant, s

t = Time, s

I = Current, A

In the RCR Table models, state of charge is a function of each set of R_O , R_P , V_O and τ parameters for a particular temperature. You specify the evolution of each parameter in the table. There are no generic equations to express the evolution of these parameters as they are data measured which varies from cell to cell. A Bezier curve or a liner interpolation is applied to calculate the evolution of the variables for the in-between table points. This model accounts for the rate-dependent resistance that is defined as:

$$R_p = R_{p,O} \left(\frac{1}{\frac{|i|}{|i_1|} + \exp\left(-\frac{|i|}{i_O}\right)} \right) \quad (2.15)$$

The diffusion and polarization resistance modifies the parallel resistance. They are defined as:

Diffusion resistance

$$R_d = A_d \sqrt{\frac{t}{e^{B_d} - e^{V_{oc}}}} \quad (2.16)$$

Where,

t = Time, s

A_d = User-specified constant

B_d = User-specified constant

V_{oc} = Open-circuit voltage at time t, V

Polarization resistance

$$R_{p,1} = R_{p,O} \left(\frac{R_{p,O}}{\frac{|i|}{|i_{p,1}|} + \exp\left(-\frac{|i|}{i_{p,O}}\right)} \right) \quad (2.17)$$

Where,

i = Local unit cell current density, A/m²

$i_{p,0}$ = User-specified constant, A/m²

$i_{p,1}$ = User-specified constant, A/m²

The algorithm used for development of RCR model is robust enough to reasonably deliver accurate results even if there were mistakes while specifying the initial state of charge, however for best results is it best to base the model on empirical test results.

2.2 CFD Modelling

Most of the fluid flows that are of engineering interest are characterized by quantities that are irregularly and fluctuating. High frequency and small scale nature of

these qualities makes it computationally expensive to resolve them in space and time. Instead of using direct numerical simulation (DNS) it becomes far less expensive to solve them for filtered or average quantities and model the impact of the small fluctuating structures. Turbulence modeling provides different approaches for modeling these small structures. Reynolds-Averaged Navier-Stokes (RANS) turbulence models provide closure relations for RANS equations. To obtain the RANS equations, the solution variable in instantaneous NS equation is decomposed into two parts, the mean or the averaged part and the fluctuating part.

$$\phi = \bar{\phi} + \phi' \quad (2.18)$$

where ϕ represents pressure, energy, velocity, or species concentration. The equation for the mean quantities can be obtained after inserting the decomposed solution variables into the N-S equation

The mean momentum and mass transport equations can be written as:

$$\frac{\partial(\rho\bar{v})}{\partial t} + \nabla \cdot (\rho\bar{v} \otimes \bar{v}) = -\nabla \cdot p\bar{I} + \nabla \cdot (T + T_t) + f_b \quad (2.19)$$

$$\frac{\partial\rho}{\partial t} + \nabla \cdot (\rho\bar{v}) = 0 \quad (2.20)$$

where:

I = identity tensor

T = viscous stress tensor

T_t = Reynolds shear stress tensor

The Reynolds shear stress tensor is defined as

$$T_t = -\rho \begin{pmatrix} \overline{u'u'} & \overline{u'v'} & \overline{u'w'} \\ \overline{u'v'} & \overline{v'v'} & \overline{v'w'} \\ \overline{u'w'} & \overline{v'w'} & \overline{w'w'} \end{pmatrix} \quad (2.21)$$

The Reynolds stress tensor can be modelled as a function of mean flow quantities by the Boussinesq approximation

here,

$$T_t = 2\mu_t S - \frac{2}{3}(\mu_t \nabla \cdot \bar{v}) I \quad (2.22)$$

where,

S = mean strain rate tensor

$$S = \frac{1}{2}(\nabla \bar{v} + \nabla \bar{v}^T) \quad (2.23)$$

\bar{v} = mean velocity

I = identity tensor

The eddy viscosity model are based on the relationship between the turbulent motion and molecular gradient-diffusion. The Reynolds stress tensor is modelled based on the concept of turbulent eddy viscosity. Some models rely on the mixing length concept to model the turbulent viscosity, the eddy viscosity models solve for additional transportation terms. The anisotropy of turbulence is not considered when we assume the Reynold stress tensor is directly proportional to the mean strain, in order to account for such anisotropy two equation models are developed.

2.2.1 Standard k- ϵ and realizable k- ϵ model

The first two-equation turbulence model considered in our study is the k- ϵ turbulence model it solves for the transport equations for the turbulent dissipation rate ϵ

and the turbulent kinetic energy so as to determine the turbulent eddy viscosity.

Is it one of the most widely used model in the industry, the original k- ϵ model was developed by Jones and Launders [37] there are various forms of the k- ϵ turbulence model developed, since the inception of the model there has been several modifications to improve it's accuracy. We are considering the standard k- ϵ model [38] and the realizable k- ϵ [39] model in this study.

The turbulent viscosity for this model is determined by the equation below

$$\mu_t = \rho C_\mu f_\mu k T \quad (2.24)$$

where:

C_μ is a Model Coefficient

f_μ is a Damping Function

T is the turbulent time scale

There is a difference in the method in which the turbulent time scale is modelled for the k- ϵ and the realizable k- ϵ model.

Transport equation:

$$\frac{\partial(\rho k)}{\partial t} + \nabla \cdot (\rho k \bar{v}) = \nabla \cdot \left[\left(\mu + \frac{\mu_t}{\sigma_k} \right) \nabla k \right] + P_k - \rho(\epsilon - \epsilon_0) + S_k \quad (2.25)$$

$$\frac{\partial(\rho \epsilon)}{\partial t} + \nabla \cdot (\rho \epsilon \bar{v}) = \nabla \cdot \left[\left(\mu + \frac{\mu_t}{\sigma_\epsilon} \right) \nabla \epsilon \right] + \frac{1}{T_e} C_{\epsilon 1} P_\epsilon - C_{\epsilon 2} f_2 \rho \left(\frac{\epsilon}{T_e} - \frac{\epsilon_0}{T_0} \right) + S_\epsilon \quad (2.26)$$

\bar{v} is the mean velocity

μ is the dynamic viscosity

σ_k , σ_ϵ , $C_{\epsilon 1}$ and $C_{\epsilon 2}$ are the Model Coefficients

P_k and P_ϵ are the Production terms

f_2 is a Damping Function

S_k and S_ϵ are the user-specified source terms

The production terms for the $k - \epsilon$ model and realizable $k - \epsilon$ model are defined differently.

Production term for standard $k - \epsilon$ two layer

$$P_k = G_k + G_{nl} + G_b + \gamma_M \quad (2.27)$$

$$P_k = G_k + G_{nl} + C_{\epsilon 3} G_b + \frac{\rho}{C_{\epsilon 1}} \gamma_y \quad (2.28)$$

Production term for realizable $k - \epsilon$ model two layer

$$P_k = f_c G_k + G_b + \gamma_m \quad (2.29)$$

$$P_k = f_c S k + C_{\epsilon 3} G_b \quad (2.30)$$

G_k = turbulent production

G_b = buoyancy production

G_{nl} = non-linear production

f_c = curvature correction factor

$C_{\epsilon 3}$ = model coefficient

γ_M = compressibility modification

γ_y = yap correction

2.2.2 SST k - ω model

The SST k- ω model is a modified version of the two-equation K-Omega turbulence model, majority of the work on the standard k-omega model was done by Willcox [40], and the SST k-omega model development was by Menter [12]. The k- ω model determines the turbulent eddy viscosity by solving the equations for specific dissipa-

tion rate ω and the turbulent kinetic energy, k . ω is defined as dissipation rate per unit kinetic energy (TKE) ($\omega \propto \epsilon/k$)

One of the biggest advantage of the k-omega model is its improved performance for analyzing the boundary layer under adverse pressure gradients. The biggest disadvantage of the model is the sensitivity to omega in free stream. Hence to overcome this disadvantage Menter [12] proposed a blending function that would include a cross-diffusion term far from the wall, but not near the boundary. this methods effectively blends the k-omega near the wall and the k-epsilon model in the far-field region.

Turbulent eddy viscosity

$$\mu_t = \rho k T \quad (2.31)$$

where,

ρ = density

T = turbulent time scale

Transport equations

$$\frac{\partial(\rho k)}{\partial t} + \nabla \cdot (\rho k \bar{v}) = \nabla \cdot \left[\left(\mu + \frac{\mu_t}{\sigma_k} \right) \nabla k \right] + P_k - \rho \beta^* f_{\beta^*} (\omega k - \omega_0 k_0) + S_k \quad (2.32)$$

$$\frac{\partial(\rho \omega)}{\partial t} + \nabla \cdot (\rho \omega \bar{v}) = \nabla \cdot [(\mu + \sigma_\omega \mu_t) \nabla \omega] + P_\omega - \rho \beta f_\beta (\omega^2 - \omega_0^2) + S_\omega \quad (2.33)$$

where,

\bar{v} = mean velocity

μ = dynamic viscosity

$\sigma_k, \sigma_\omega, C_{\epsilon 1}, C_{\epsilon 2}$ = model coefficients

$P_k, P_\omega =$ Production terms

where,

$$P_k = G_k + G_{nl} + G_b \quad (2.34)$$

$$P_\omega = G_\omega + D_\omega \quad (2.35)$$

here

$G_k =$ turbulent production

$G_b =$ buoyancy production

$G_{nl} =$ non-linear production

$G_\omega =$ specific dissipation production

$D_\omega =$ cross diffusion term.

2.2.3 Elliptic Blending model

The elliptic Blending model solves for eddy viscosity by considering the turbulent kinetic energy, turbulent dissipation energy, elliptic blending factor, and the wall-normal stress component. Durbin [41] in 1991 proposed the concept of elliptic relaxation for Reynolds stress models. This led to the development of the Elliptic Blending model, it is considered to be an improvement on the k-epsilon model in terms of near wall analysis and the k-omega model in terms of stability.

Turbulent viscosity

$$\mu_t = \rho_\mu \varphi k \min \left(T, \frac{C_T}{\sqrt{3} C_\mu \phi S} \right) \quad (2.36)$$

where

$C_\mu, C_T =$ model coefficients

$T =$ turbulent time scale

Transport equations:

$$\frac{\partial(\rho k)}{\partial t} + \nabla \cdot (\rho k \bar{v}) = \nabla \cdot \left[\left(\frac{\mu}{2} + \frac{\mu_t}{\sigma_k} \right) \nabla k \right] + P_k - \rho(\epsilon - \epsilon_0) + S_k \quad (2.37)$$

$$\frac{\partial(\rho \epsilon)}{\partial t} + \nabla \cdot (\rho \epsilon \bar{v}) = \nabla \cdot \left[\left(\frac{\mu}{2} + \frac{\mu_t}{\sigma_\epsilon} \right) \nabla \epsilon \right] + \frac{1}{T_e} C_{\epsilon 1} P_\epsilon - C_{\epsilon 2}^* \left(\frac{\epsilon}{T_e} - \frac{\epsilon_0}{T_0} \right) + S_\epsilon \quad (2.38)$$

$$\frac{\partial(\rho \varphi)}{\partial t} + \nabla \cdot (\rho \varphi \bar{v}) = \nabla \cdot \left[\left(\frac{\mu}{2} + \frac{\mu_t}{\sigma_\varphi} \right) \nabla \varphi \right] + P_\varphi + S_\varphi \quad (2.39)$$

$$\nabla \cdot (L^2 \nabla \alpha) = \alpha - 1 \quad (2.40)$$

\bar{v} = mean velocity

μ = dynamic viscosity

$P_k, P_\epsilon, P_\varphi$ = Production terms

$\sigma_k, \sigma_\epsilon, \sigma_\varphi, C_{\epsilon 1}$ and $C_{\epsilon 2}^*$ = Model Coefficients

Production terms are defined as

$$P_k = G_k + G_b + \gamma_M \quad (2.41)$$

$$P_\epsilon = C_{\epsilon 3} G_b + \frac{1}{C_{\epsilon 1}} E \quad (2.42)$$

$$P_\varphi = -\frac{\varphi}{k} (G_k + G_b) + \rho(1 - \alpha^3) f_w + \rho \alpha^3 f_h \quad (2.43)$$

G_k = turbulent production

G_b = buoyancy production

$C_{\epsilon 3}$ = model coefficient

E = additional production

As we are conducting URANS simulations a transient term an additional coordinate of time needs to be added. The Euler implicit scheme with a first order temporal scheme is used for approximating the transient term. The current time level is given by "n+1" and the previous time level as "n"

$$\frac{d}{dt}(\rho\varphi V)_0 = \frac{(\rho\varphi V)_0^{n+1} - (\rho\varphi V)_0^n}{\Delta t} \quad (2.44)$$

CHAPTER 3: NUMERICAL SETUP

This chapter explains the details related to the numerical setup, for all the simulations carried out in this study. The set-up was developed after analyzing the knowledge gathered by successive testing. Few of the settings that were constant throughout the study are, the commercial tool used for finite volume analysis, i.e STAR-CCM+ and the tool used for battery designing, Battery design studio.

The initial cases that were used for conducting the 2D analysis to study the domain set-up and flow-field analysis were run using STAR-CCM+ v13.04 and the final 3D simulations were conducted in STAR-CCM+ v15.04. All the simulations used implicit unsteady, segregated fluid temperature and segregated flow solvers utilizing SIMPLE algorithm.

To accelerate solver convergence an Algebraic Multi-grid (AMG) linear solver is used with a combination of V cycle for the pressure value and F cycle for velocity is utilized.

3.1 Battery set-up

The battery was designed using the distributed model [28] in BDS. Distributed model is a purely empirical model, a detailed model of the battery can be designed using this model. The model has the highest accuracy in modelling a battery in comparison with the NTG and RCR model. The NTG [31], [33] and RCR model [35], [36] requires values of admittance vs voltage and resistance vs state of charge respectively to model the numerical model. The independence of the distributed model from experimental data makes it an ideal choice for numerical analysis.

It accounts for the liquid-phase mass balance, solid-phase mass balance, kinetic

parameters, solid and liquid state diffusion process. All these considerations allows the Distributed model to make accurate prediction of the battery performance.

The battery considered in our study is a lithium-ion battery, they are less toxic when compared with nickel-cadmium or lead-acid battery. The disposal of the LIB also has less impact on the environment. A typical LIB consists of a negative lithium electrode, an electrolyte and a positive electrode in our case it is Nickel-Manganese-Cobalt (NCM - 811), it is commercially known as the LG INR18650 MJ1. The specifications for this battery are as follows:

Table 3.1: Battery specification [1]

Parameter	Value
Model	LG INR 18650 MJ1
Active Material	$LiNiCoMnO_2$
Nominal Voltage (V)	3.635
Nominal Capacity (Ah)	3.5
Minimum Capacity	3.4
Cut off voltage (V)	2.5
Operating temperature (charging) °C	0 - 45
Operating temperature (discharging) °C	-20 to 60
Weight (g)	49

The battery was designed in BDS while keeping these parameters in consideration. As battery design studio conducts detail modelling of a cell, the parameters required for designing the cell were taken from [2]. The battery details were characterized using calorimetry, open-circuit potential experiments and infrared thermography.

Table 3.2: Parameterization of NMC-811/SiC electrodes [2]

Parts	Silicon-graphite SiC	Separator	Nickel-rich NMC-811
Thickness	86.7 μm	12 μm	66 μm
Particle Radius R_p	6.1 μm		3.8 μm
Active material %	69.4%		74.5 %
Inactive fraction	9 %		8.4 %
Buggerman coeff. β	1.5	1.5	1.85
Porosity ε_l	21.6 %	45 %	17.1 %
Stoichiometry 100%	0.852		0.222
Stoichiometry 0%	0.002		0.942
Density ρ	2.24 g cm ⁻³		4.87 g cm ⁻³

The battery pack which consists of 32 cells connected in 4p8s (four in parallel and eight in series) arrangement. A cycler was designed to charge and discharge the cells with a specified current value and time-period. The cycler current value for 1C discharge was 13.4 A and for 2C discharge the current value was 26.8 A.

The configurations for which this study is conducted are, the staggered, aligned and cross arrangement. Design parameters of the battery pack are as shown in the table below

Table 3.3: Battery pack design parameters [1]

Parameter	Aligned	Staggered	Cross
Distance between two cells (mm)	22	22	22
Cell diameter (mm)	18	18	18
Cell height (mm)	65	65	65
Distance between cell and wind-tunnel wall (mm)	13	13	13

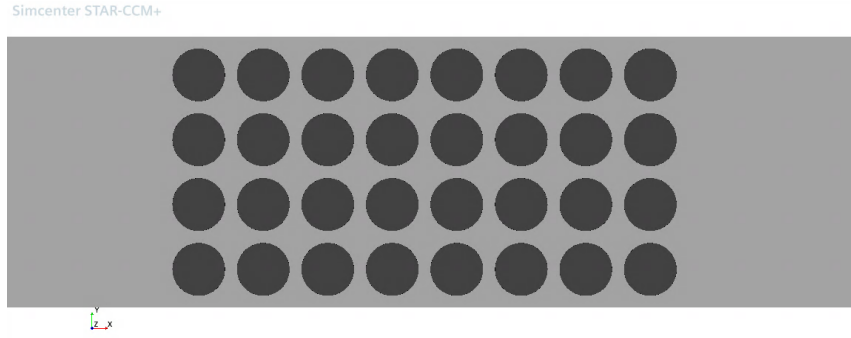


Figure 3.1: Aligned geometry

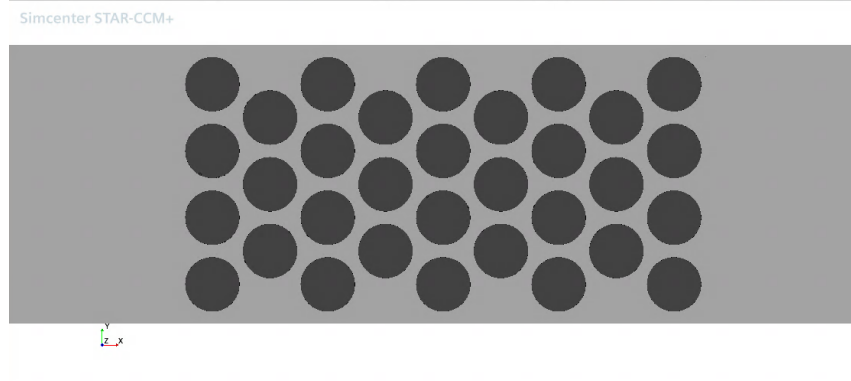


Figure 3.2: Staggered geometry

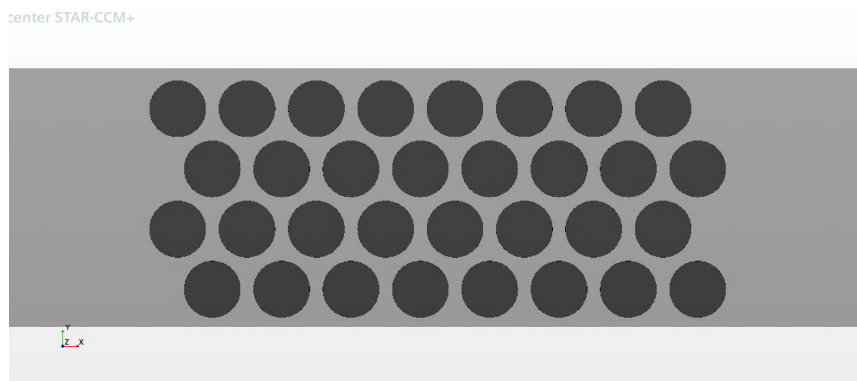


Figure 3.3: Cross geometry

The space utilization which is used for determining how densely packed the batteries are, is determined as the ratio of the volume occupied by the battery cells to the volume of the whole battery pack (including the air space), the percentage for the three arrangements while keeping design parameters constant are as follows:

- Aligned - 49.15 %
- Staggered - 49.58 %
- Cross - 51.24 %

The cross arrangement has the highest space utilization percentage. It is the most densely packed battery arrangement. The three battery pack arrangements are tested to determine the most efficient way of cell packaging.

3.2 2D Analysis

2-Dimensional (2D) simulations help us in understanding the general layout of the simulation before we move to 3-dimensional (3D) simulations, also the time required for running a 2D simulation is substantially less compared to 3D simulations. To design the shape and dimension of the external domain we studied the flow field development in 2D first. The first step was constructing the wind-tunnel used in experiment, the wind-tunnel dimensions were taken from the experimental paper [1]. A steady state 2D simulation is constructed, with holes punched in the shape of battery cylinders, as you can see in the figure below.

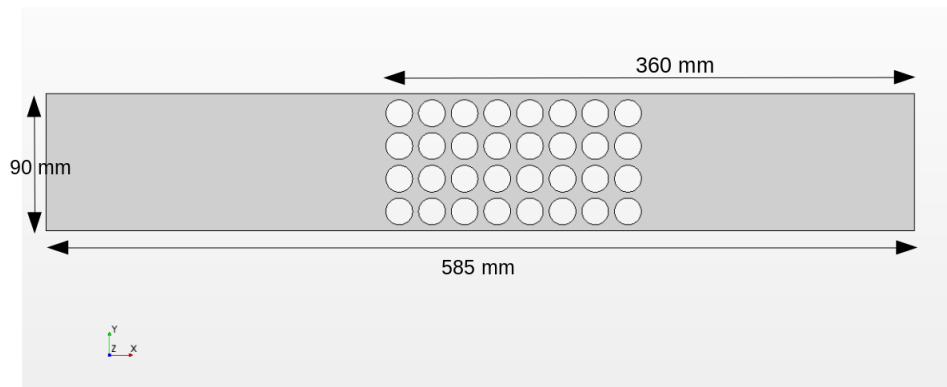


Figure 3.4: 2D steady state simulation set-up

The mesh for this analysis is kept coarse, the base size selected is 12 mm. The total mesh size is 17784 cells. The mesh near the punched holes and the wake region is

refined. As not much turbulence is expected near the inlet the mesh is coarser there. The meshers used are trimmed cell mesher, prism layer mesher and surface remesher.

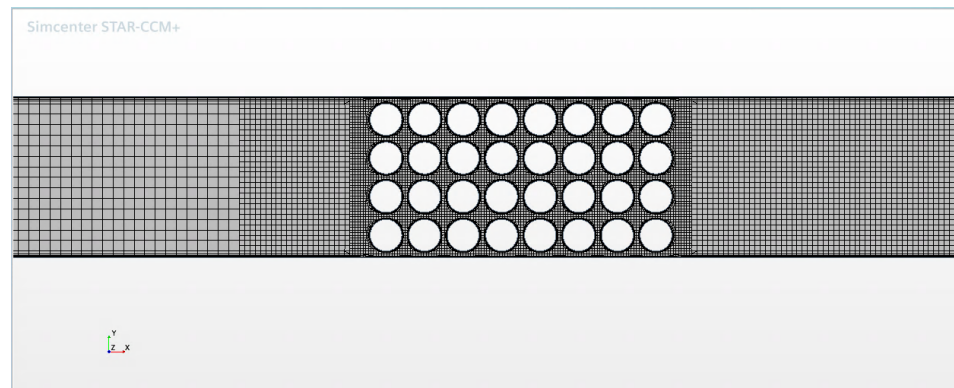


Figure 3.5: Mesh scene for 2D set-up

After observing the velocity Figure 3.2 and pressure scalars Figure 3.3, gradients were observed in the wake region and near the wind-tunnel outlet, these gradients would make the simulation highly unstable.

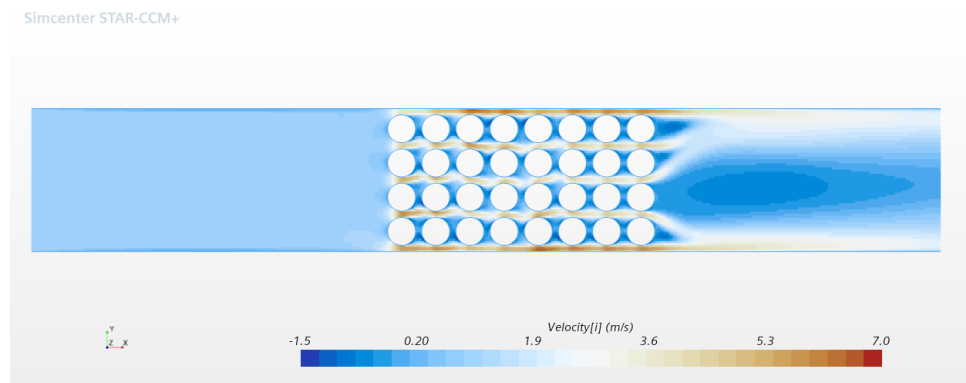


Figure 3.6: Velocity plot for 2D set-up

The blockage ratio for our object which is defined as the ratio of the frontal area of the object to the cross-section area of the wind-tunnel value is 0.782. The effect of high-blockage ratio can be seen in the increase in velocity value. A jet like structure is formed between the rows of the cells.

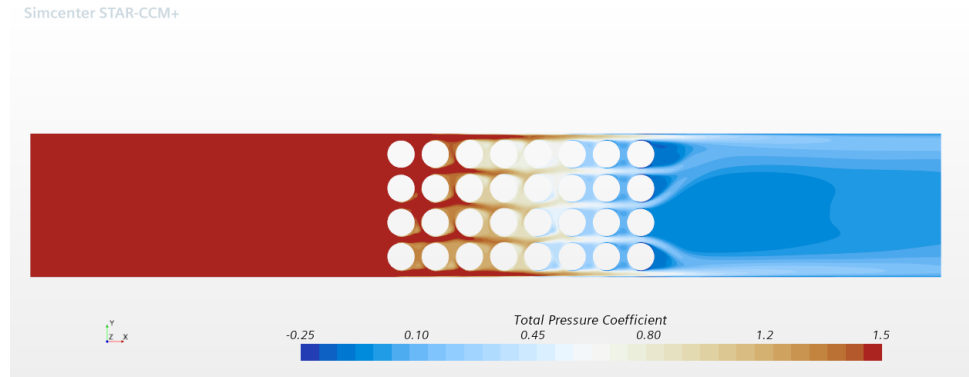


Figure 3.7: Total pressure coefficient for 2D set-up

The scalar scene above shows the total pressure coefficient at the outlet, the total pressure coefficient value varies from 0.45 to -0.2, these pressure and velocity gradients at the outlet makes the simulation highly unstable.

A Karman vortex street is observed, it is formed due to the vortex shedding caused by flow separation of unsteady flow near blunt bodies. The dimensions of the wind-tunnel cannot be changed, as to maintain with the consistency of the results concerning the experiment. But as we can see from the velocity Figure 3.2 and pressure Figure 3.3, our outlet needs to be modelled in such a fashion so that it can reduce the gradients near the outlet.

The boundary conditions for the battery numerical simulations are usually not elaborately mentioned in literature work [19], [42], in this work we are emphasizing the outlet condition for the wind-tunnel, a plenum is included as part of the domain in the downstream direction. It is made to be large enough so that at the outlet boundary condition there are no propagating disturbance waves, it also helps in relating the numerical simulation to more realistic conditions and forms as the core for making the simulations highly stable. The boundary condition for all the walls of the plenum is pressure outlet.

An extension of the wind-tunnel is added in the upstream direction, the boundary conditions for this extension includes wall with slip condition and velocity inlet.

The upstream extent of the computational domain is extended for development of a smoother boundary layer. It is a method commonly utilized in boundary flow numerical simulations [43], [44].

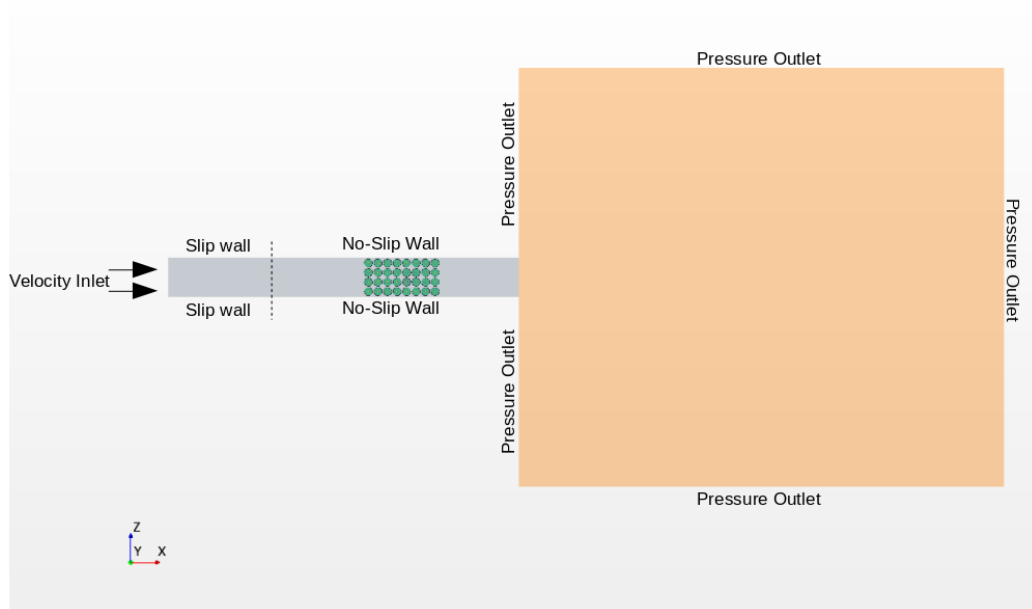


Figure 3.8: Layout

3.3 3D Analysis

CFD is a compromise between cost-efficiency and accuracy, this balance plays an important role during mesh size and time-step selection. Unless there is substantial change in results, we do not go for a finer size mesh as it becomes computationally expensive. To study the effect of mesh dependence on the final results we conduct a study in which we run the simulations with $\pm 20\%$ and $\pm 10\%$ around the initial value selected. A plot of number of cells vs the change in quantity to be observed is plotted. After studying the plot a final decision of the mesh base size is done. For our case we conducted a mesh refinement study at 2C discharge rate for an inlet velocity of 1m/s. In the table below shows the effect of mesh base size on maximum temperature, minimum temperature and drag coefficient, after comparing the values, we went forward with a base size of 10.8 mm.

Table 3.4: Mesh independence study

Mesh size (mm)	Number of cells	Drag coefficient	Maximum Temperature (K)	Minimum Temperature (K)
8.4	56.03 million	30.1	312.45	300.99
9.6	38.74 million	30.09	312.38	300.98
10.8	28.10 million	30.07	312.43	300.84
12	20.68 million	29.55	312.3	300.87
13.2	17.63 million	28.87	312.86	301.34

The mesh specification for this study are as follows:

- The solvers used for mesh generation are surface remesher, trimmed cell mesher, automatic surface repair and prism layer mesher
- Trimmed cell mesher is used because it is fast and high quality, gives anisotropic refinement and is perfect for large domains
- Volume controls are used to refine the regions near the battery and to capture the wake region, Figure 3.5 shows the mesh development with help of the volume control. As the mesh transitions from the wind-tunnel to the plenum the volume control make the mesh coarser. This helps in reducing the computational cost.

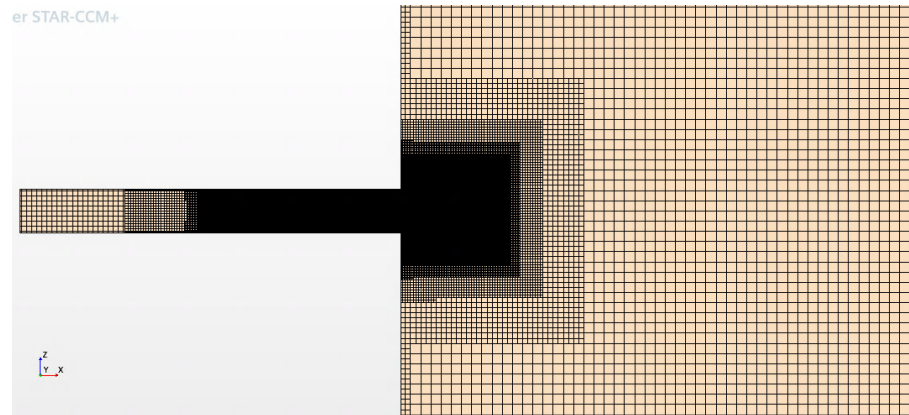


Figure 3.9: Volume controls

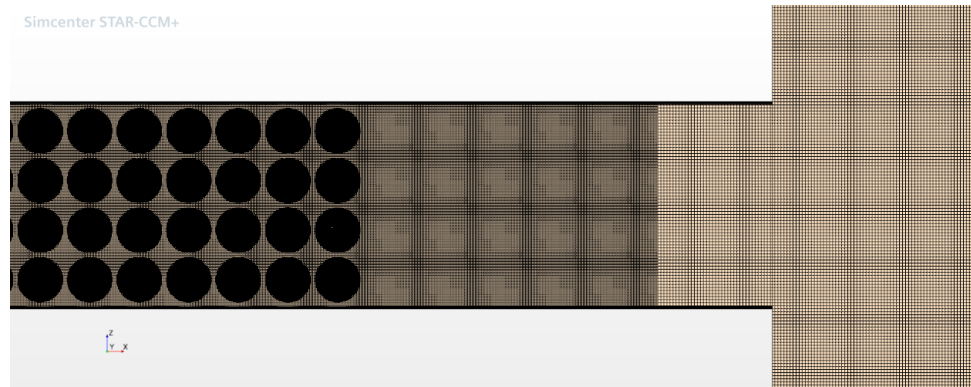


Figure 3.10: Wake refinement

- Prism layer mesher is used to improve the precision of the prediction of flow features for example the drag, resolving of the velocity and temperature gradient near the wall. These gradients are much sharp at the viscous sub-layer in comparison with rest of the flow field, a coarser mesh would be unable to capture them properly.

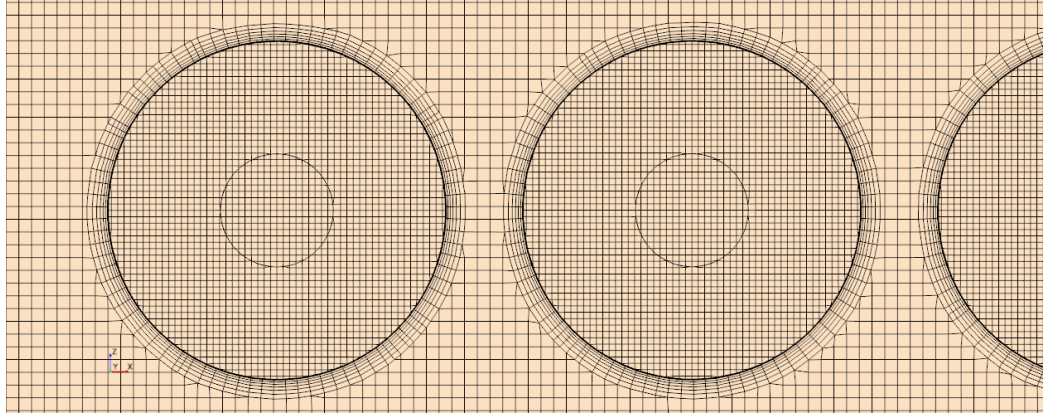


Figure 3.11: Prism Layers development around the battery

Unsteady simulation is chosen here because we have time dependent heat-source, and it is a transient heat transfer simulation. The time step selection for the unsteady simulation is based on the Courant–Friedrichs–Lewy or the CFL condition or CFL number. CFL number is a dimensionless quantity. It is defined as $c = u\Delta t/\Delta x$ where u is the velocity, Δt is the time-step and Δx is mesh size. For the simulation to be stable, a CFL number of 1 is suggested. As the total time for which we are running the simulation is high, we conducted a time step study to determine the ideal time-step. Initially a CFL of 2000 was chosen (time-step 2s) and we tested till CFL number of one magnitude less, after observing the maximum and minimum temperature values, and the drag values, it was observed there is not much change as we decrease the time-step size below 1 second, hence the time-step size 1 second was found to be ideal. The CFL for this time-step is 1000, it is higher than the traditionally accepted values but as there was no change in results for lower time-steps we can assume that the time-step size is sufficient to capture all frequencies of interest.

Table 3.5: Time-step independence study

Time step (s)	Drag coefficient	Maximum Temperature (K)	Minimum Temperature (K)
4	30.85	311.61	300.96
2	30.84	312.81	300.89
1	30.07	312.43	300.84
0.5	30.17	312.42	300.85
0.25	30.1	312.46	300.84

CHAPTER 4: RESULTS AND DISCUSSION

The numerical analysis involves study of the $k - \epsilon$, Realizable $k - \epsilon$, SST and Elliptic blending model. The battery pack consisting of 32 cells in 4p8s (4 in parallel, 8 in series) arrangement are discharged with a constant current value. The battery is fully charged, we run the simulation from 100 % SOC to 0 % SOC for two different discharge rates. The results from the numerical analysis conducted are compared with experimental work [1].

The results from the turbulence models at 2C discharge rate for inlet velocities 0.6 m/s, 1 m/s, 2 m/s, 3 m/s, and 4 m/s are compared with experiment results of Fan et.al [1]. The quantities that we are observing is the maximum temperature rise ($\Delta T_{rise,max}$) which is the maximum temperature rise within the whole pack from the initial temperature and maximum temperature difference (ΔT_{max}) which the maximum temperature difference within the battery pack at at end of the discharge cycle. These two quantities help us analyze the performance of the battery thermal management system. A good BTMS keeps the maximum temperature rise and maximum temperature difference low so as to not affect the battery working efficiency.

the $\Delta T_{rise,max}$ and ΔT_{max} are defined as

$$\Delta T_{rise} = T_{max} - T_{initial} \quad (4.1)$$

$$\Delta T_{rise,max} = \max(\Delta T_{i,rise}) \quad (4.2)$$

$$\Delta T_{rise,min} = \min(\Delta T_{i,rise}) \quad (4.3)$$

$$\Delta T_{max} = \Delta T_{rise,max} - \Delta T_{rise,min} \quad (4.4)$$

4.1 Aligned arrangement

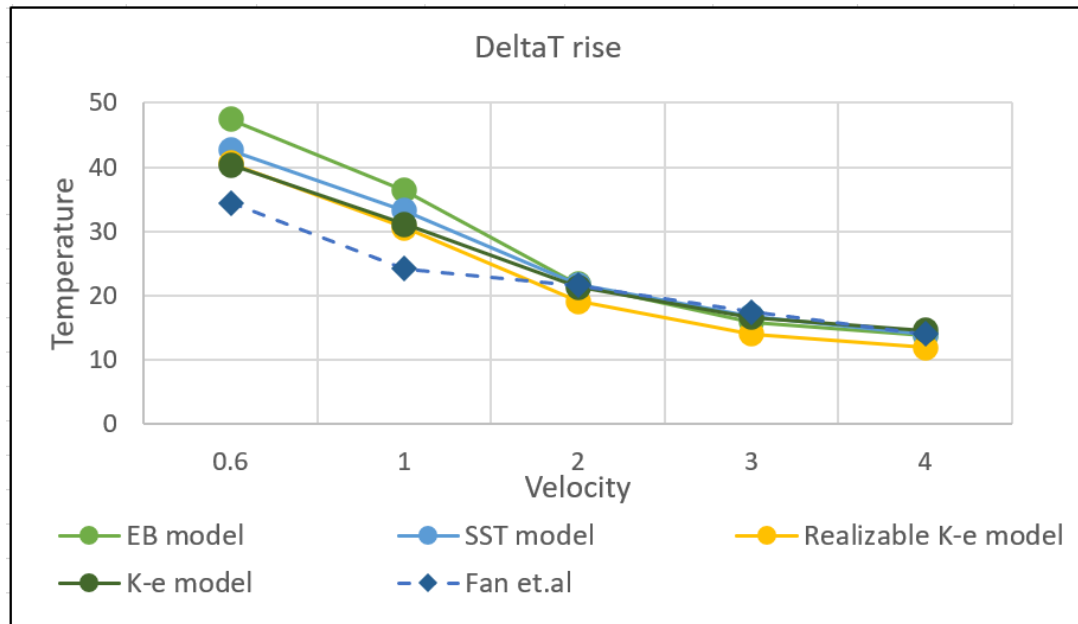
The aligned arrangement was used for comparing the results by the four turbulence models. The Figure 4.1, shows the temperature plots for $\Delta T_{rise,max}$ and ΔT_{max} it was observed that the $k-\epsilon$ model is the most appropriate model for modelling the aero-thermal behaviour of the battery pack. For low velocities we can see the model is over predicting the results, but for higher velocities the temperature predicting is in good agreement (3% - 10%)

The elliptic blending and the SST model showed promising results for higher velocities, but was over-predicting by 37% for low velocities. The realizable $k-\epsilon$ model over-predicts with the same percentage as $k-\epsilon$ model (28%) for lower velocities but for higher velocities it starts under-predicting the temperature values. Hence after all these observations it was concluded that the $k-\epsilon$ model is the most appropriate model for such simulation.

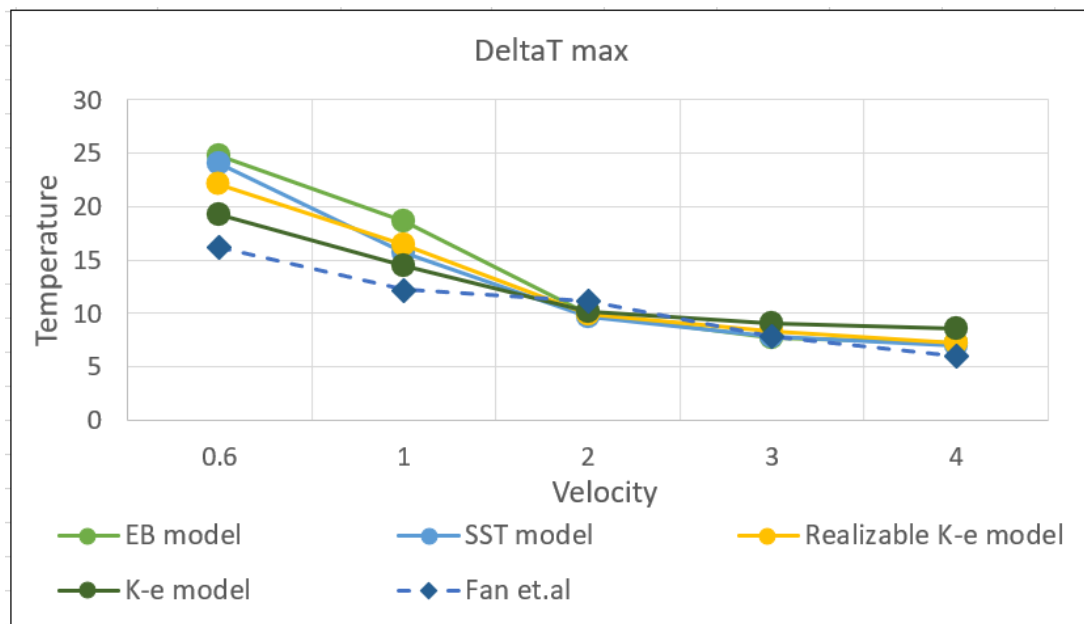
There have been several publications with similar conclusion about the $k-\epsilon$ model and it's capability to model heat transfer problems [45], [46].

There is an over-prediction of temperature observed for low inlet velocities the reason for such behavior can be a result of the following:

As the value inlet velocity is very low, the flow can be considered as natural convection rather than forced convection. While modelling natural convection there have been several studies conducted which show the inability of the turbulence models chosen in our study to predict high accuracy results [47], [48]. There are treatments recommended for increasing the accuracy of the turbulence models, the turbulent heat flux are the algebraic flux model (AFM), differential flux model, and the generalized gradient diffusion hypothesis (GGDH). The elliptic-blending second-moment closure model and the elliptic-relaxation are few of the models which are recommended for modeling natural convection [49]. The models are out of the scope of current study and can be used in future analysis.



(a) The maximum temperature rise



(b) The maximum temperature difference

Figure 4.1: Turbulence models comparison with experimental data

Secondly, the behaviour of batteries is influenced by the ambient temperature, as the inlet velocity is low, the overall surrounding temperature increases which leads to decrease in the resistance value and this impacts the heat generation rate [15], [50].

As the heat generation (H) is directly proportional to I^2R , the overall heat generation decreases as the surrounding temperature increases.

Thirdly the flow at low velocities and having high temperature differences, becomes a buoyancy driven flow. The models in our study run on an assumption of constant density value, but the buoyancy driven flow is driven on density variation [51] this could lead to over-prediction.

The key advantage of numerical simulation is the ease at which we can obtain data for even the smallest time-step and location. There is a limit on amount of thermocouples that can be attached to a battery along the length of the battery to capture the temperature values, in numerical simulation we can have n number of probes, this allows us to capture even a slightest change in temperature. Figure 4.2 and 4.3 show the ease at which data can be captured in numerical simulations.

The figure below shows the temperature distribution for an aligned arrangement at inlet velocity of 2 m/s. This plot helps us in locating all the hot spots. The variation in temperature values of top most row and the bottom row are the result of the von-karman vortex street. There are a periodic fluctuations in the wake region observe which causes this slight temperature difference.

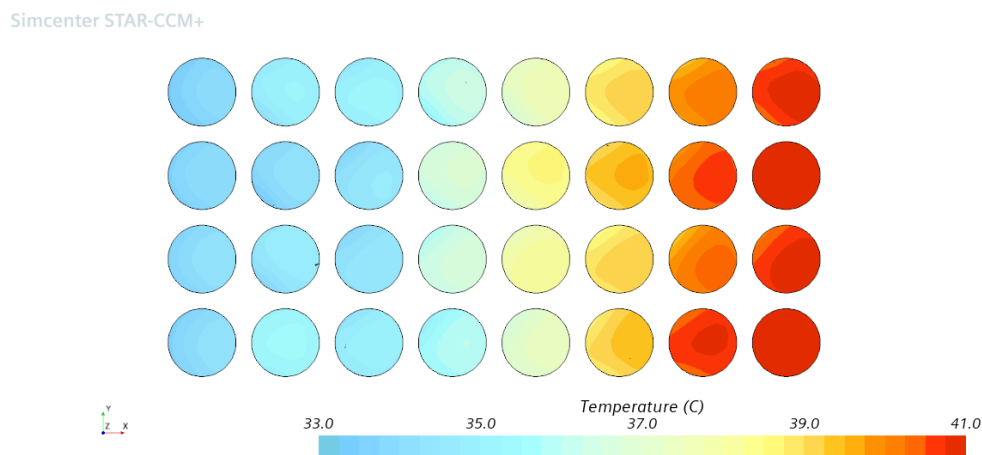
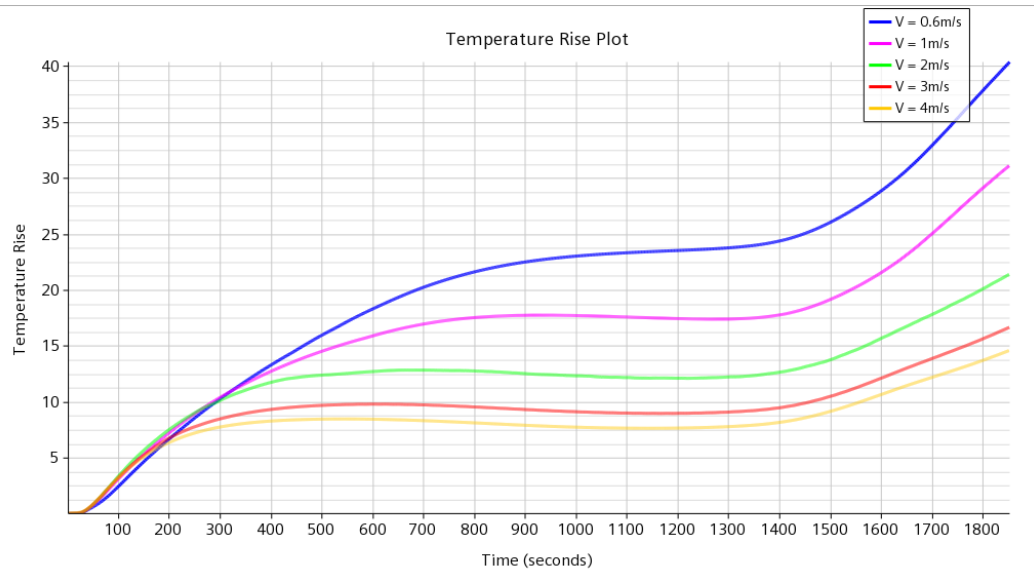


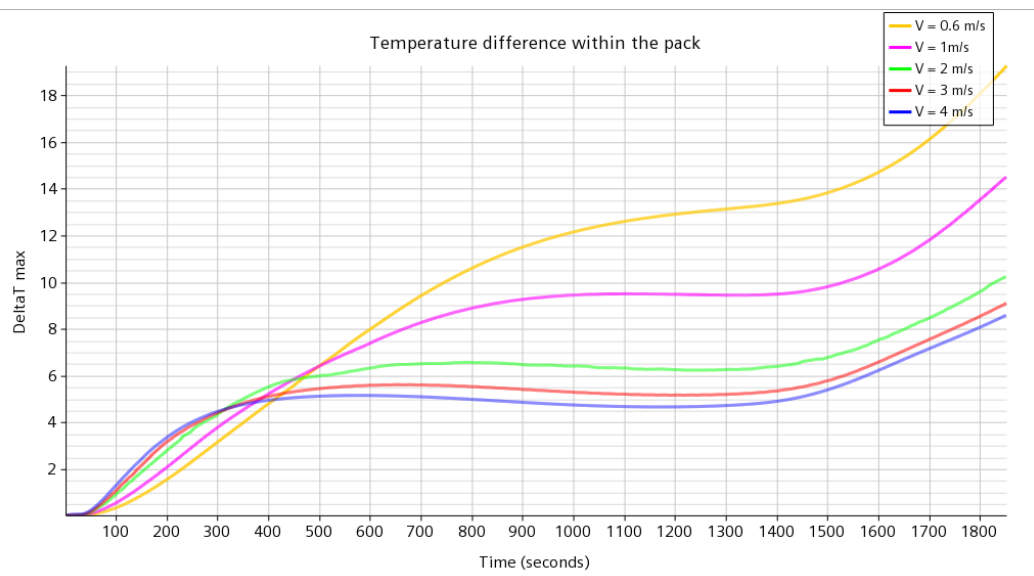
Figure 4.2: Aligned arrangement - temperature scene, inlet $V = 2$ m/s

The Figure 4.3 displays the change in $\Delta T_{rise,max}$ and ΔT_{max} for the whole run time

of the battery. The plot shows us the effect of inlet velocity on the temperature, there is a substantial drop in temperature value (10 degrees) as we move from 0.6 m/s to 1 m/s the drop in value trend gradually weakens as we further increase the velocity value, the temperature drop between 3 m/s and 4 m/s is not that high.



(a) The maximum temperature rise



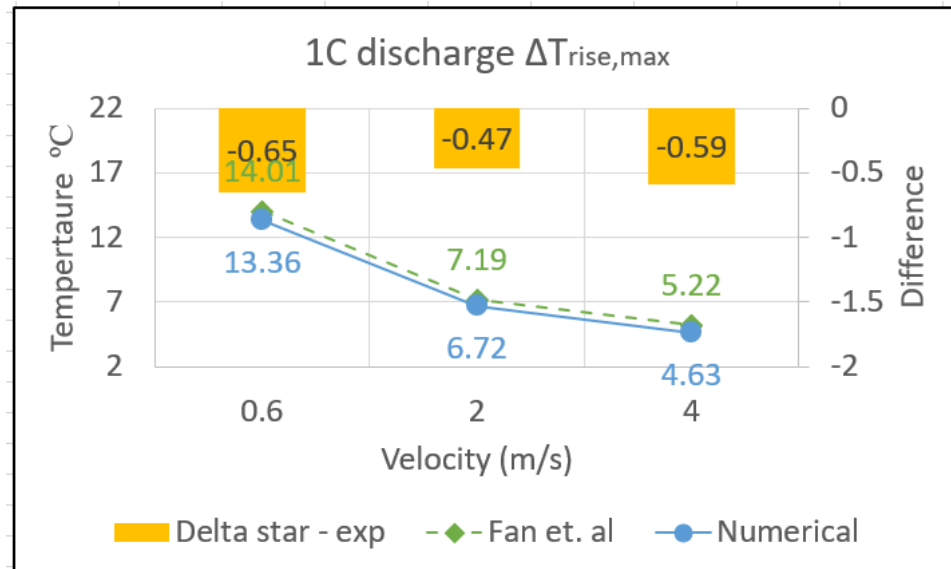
(b) The maximum temperature difference

Figure 4.3: Comparison of the temperature profile for inlet velocity 0.6 m/s to 4 m/s

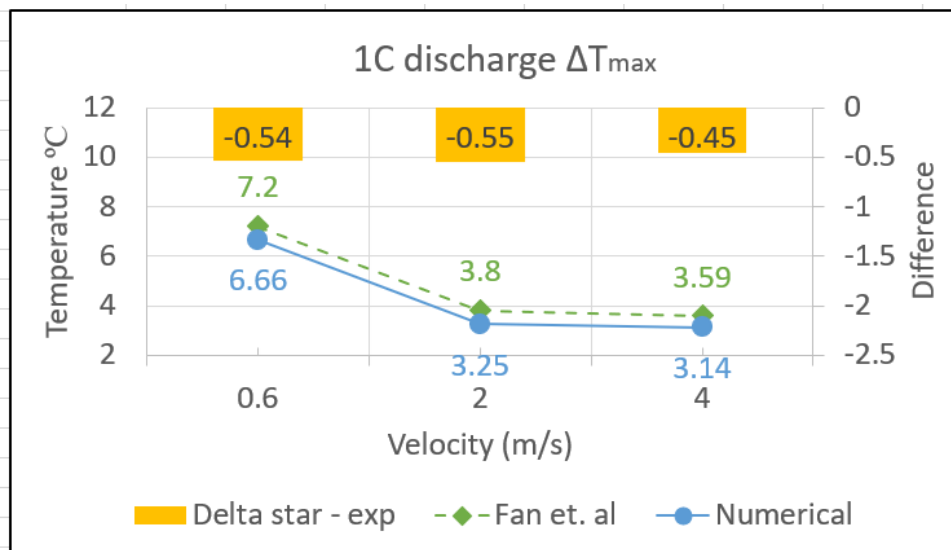
This graph helps us in choosing the optimum inlet velocity for battery cooling. The

similar trend is observed in the other plots as well.

A second simulation was conducted this time discharge rate was 1C. The Figure 4.4 show the numerical vs experiment comparison of $\Delta T_{rise,max}$ and ΔT_{max} for inlet velocities 0.6 m/s, 2 m/s and 4 m/s.



(a) The maximum temperature rise



(b) The maximum temperature difference

Figure 4.4: Comparison of maximum temperature rise and max temperature difference for 1C discharge

The results are in good alignment with the experimental data. The maximum temperature rise for a 1C discharge rate is significantly less than 2C discharge rate. There is an average 3 times decrease in temperature value compared to 2C discharge rate. As the discharge rate increases there is a near-linear trend observed in the temperature rise value.

4.2 Staggered

The staggered arrangement has the lowest space utilization ratio. The figure below shows the temperature distribution for staggered arrangement for an inlet velocity 2 m/s. The highest temperature value is observed in the last and second last column. The temperature distribution within is highly uneven.

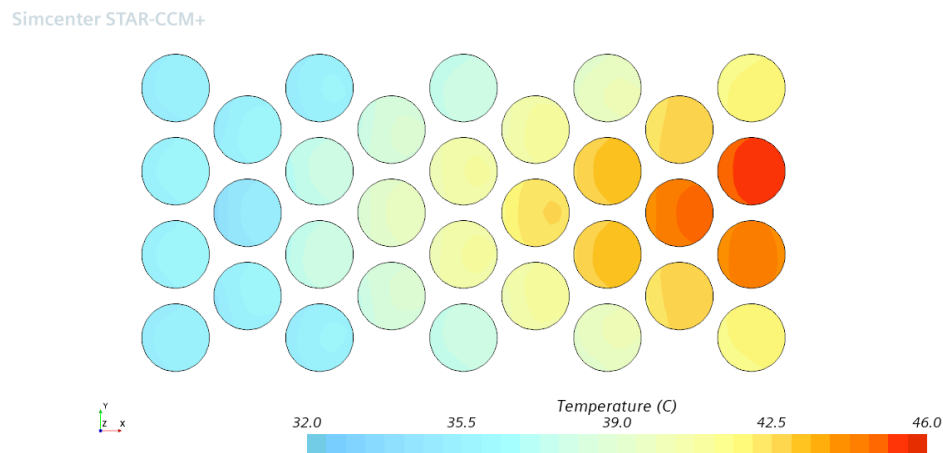
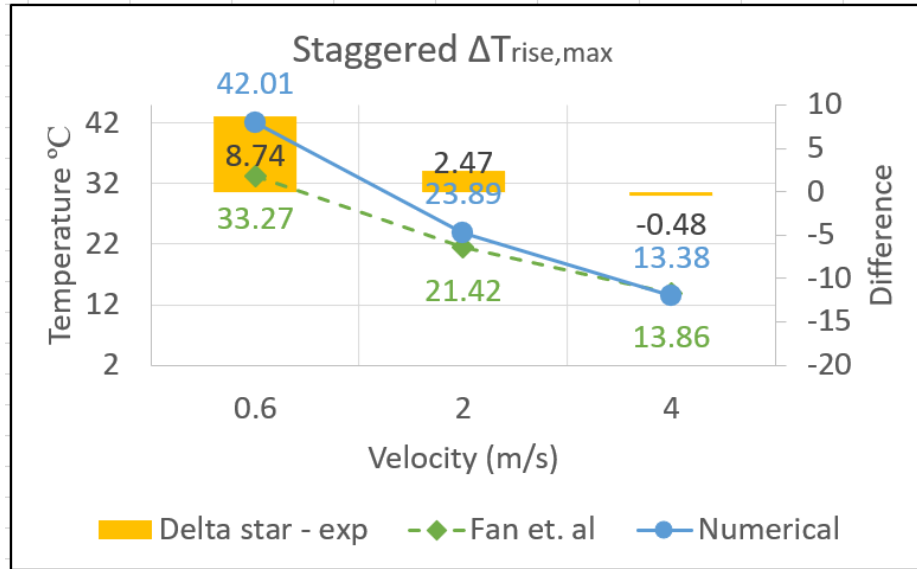
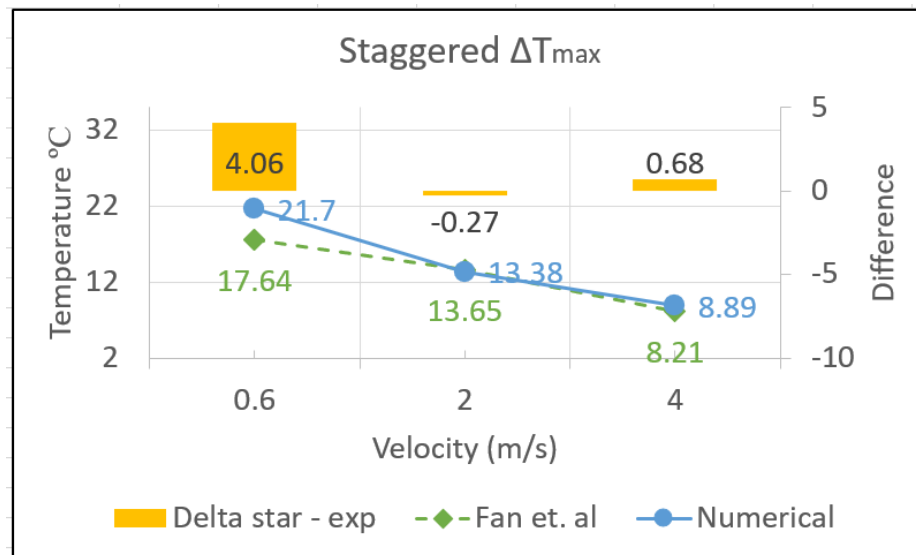


Figure 4.5: Staggered temperature scene, inlet $V = 2$ m/s

Figure 4.5 shows the temperature plot for staggered arrangement. The results from the numerical simulations are compared with experimental data Figure 4.6, a similar trend as the aligned arrangement for 2C discharge is observed. There is discrepancy observed in result for 0.6 m/s and for higher velocities the results are aligning.



(a) The maximum temperature rise

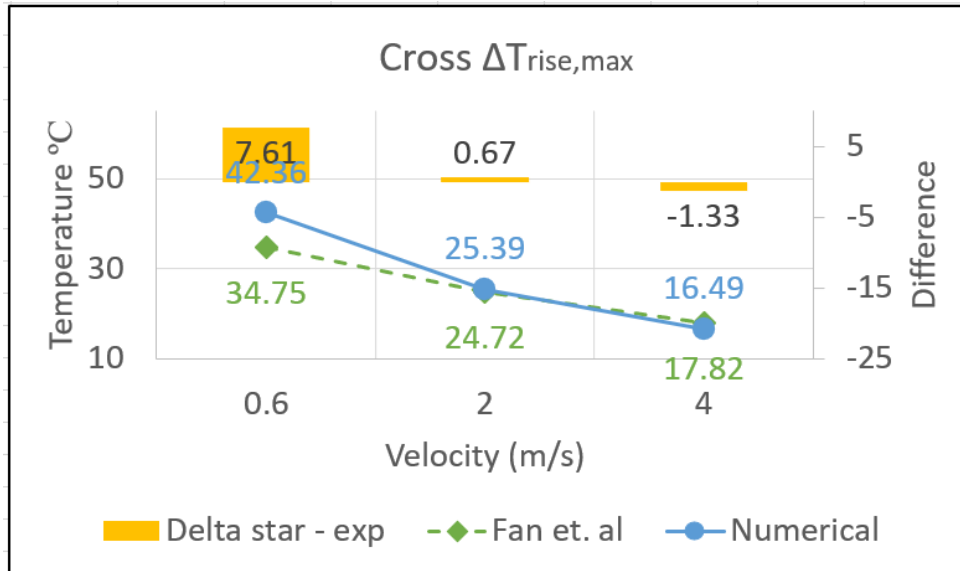


(b) The maximum temperature difference

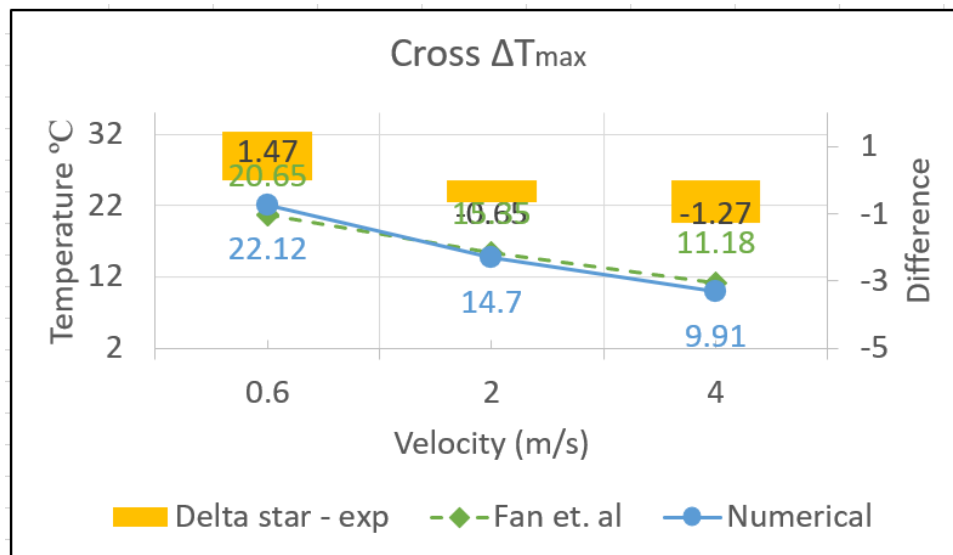
Figure 4.6: Comparison of $\Delta T_{rise,max}$ and ΔT_{max} for Staggered arrangement

4.3 Cross

The cross arrangement has the highest space utilization percentage. This type of arrangement can be used for small spaces. The Figure 4.7 shows the comparison plot of numerical data obtained in this study with experimental data.



(a) The maximum temperature rise



(b) The maximum temperature difference

Figure 4.7: Comparison of $\Delta T_{rise,max}$ and ΔT_{max} for cross arrangement

The temperature distribution as seen in Figure 4.8 has a less range in comparison with staggered arrangement. As the battery pack is densely packed the effect of this arrangement is reflected on the maximum temperature value.

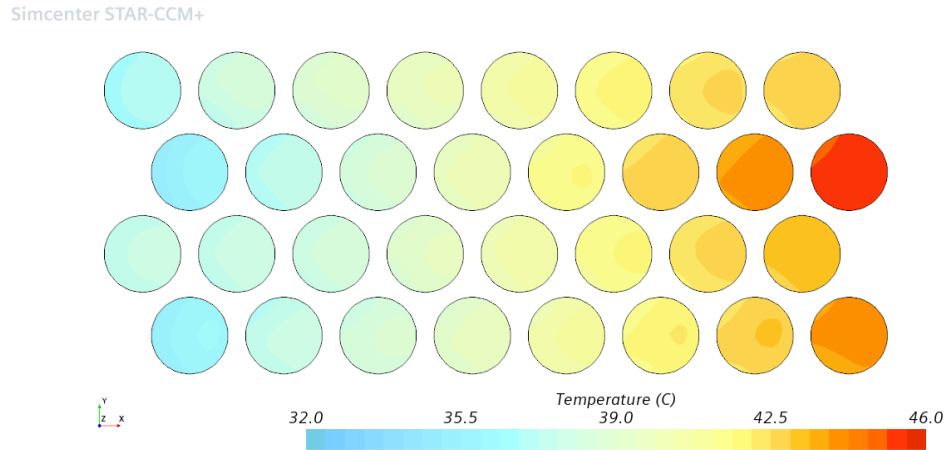


Figure 4.8: Cross arrangement temperature distribution, $V = 2$ m/s

4.4 Aligned, Staggered, and Cross arrangement

In this study three different arrangements of the battery pack are considered, aligned, staggered and cross. After running all the simulations it was confirmed that aligned arrangement has the best heat dissipation and cooling capacity. Figure 4.9 and Figure 4.10 shows the $\Delta T_{rise,max}$ and ΔT_{max} values for 0.6 m/s, 2 m/s and 4 m/s

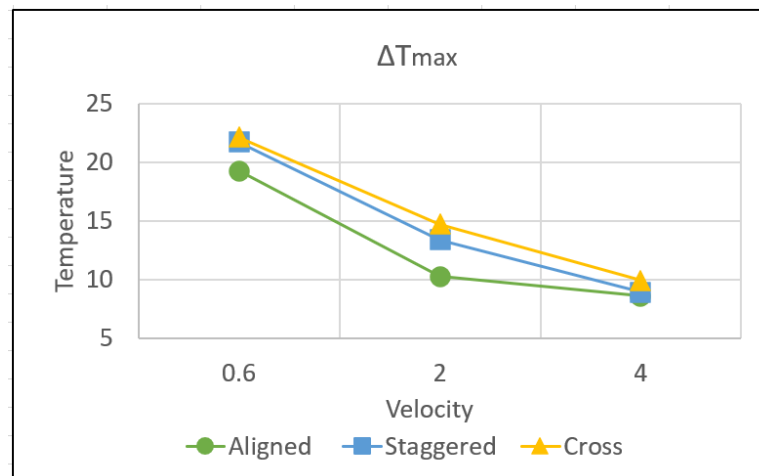


Figure 4.9: Arrangement comparison - maximum temperature, inlet $V = 2$ m/s

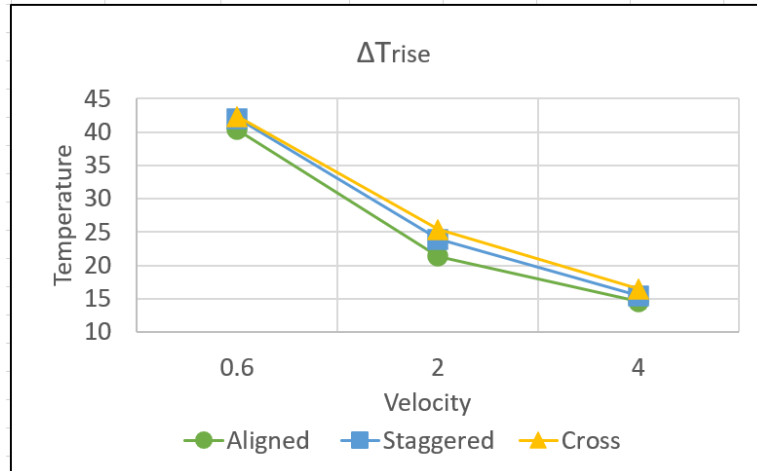


Figure 4.10: Arrangement comparison - maximum temperature rise, inlet $V = 2$ m/s

The $\Delta T_{rise,max}$ and ΔT_{max} values are less for aligned compared to staggered or cross arrangement, this can be explained if we look at the velocity and temperature scenes. For aligned arrangement the average velocity (8 m/s) is higher in comparison with staggered and cross. High velocity leads to increase in heat dissipation rate. There are few hot spots developed in the wake region of the cylinders but in comparison with other arrangements aligned performs better.

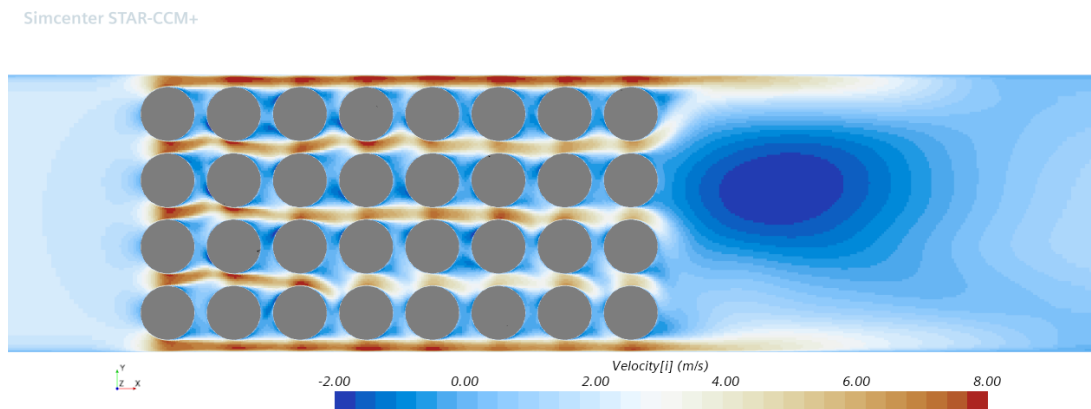


Figure 4.11: Aligned velocity scene, inlet $V = 2$ m/s

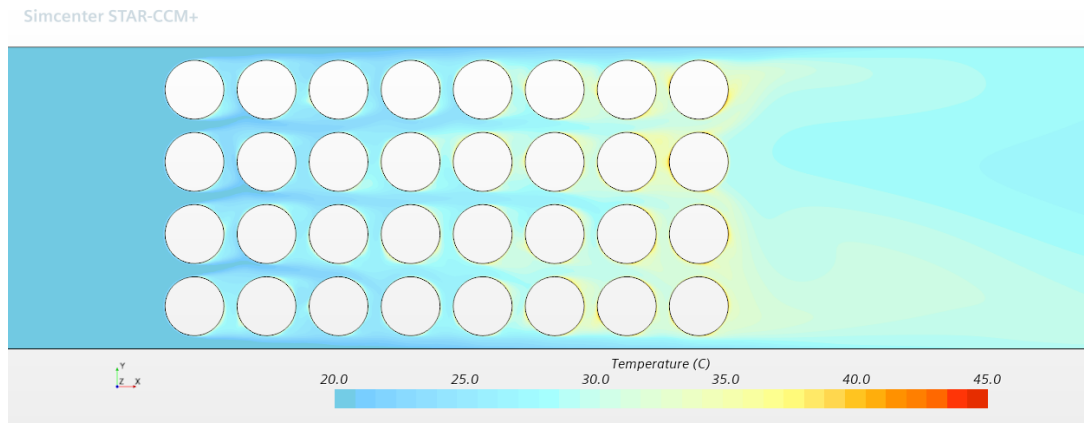


Figure 4.12: Aligned velocity scene, inlet $V = 2$ m/s

For the staggered arrangement the average velocity is in the lower range 4 m/s to 6 m/s. The battery cylinders acts as resistance to the air flow, which makes the heat dissipation difficult.

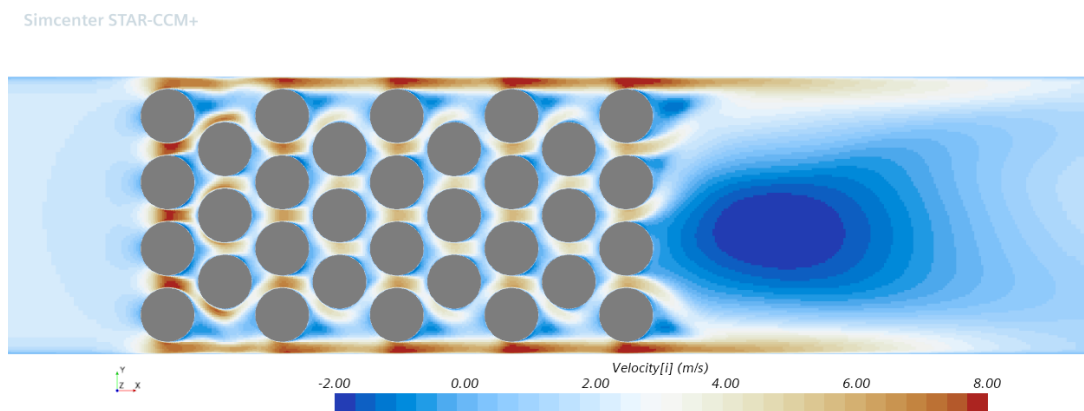


Figure 4.13: Staggered velocity scene, inlet $V = 2$ m/s

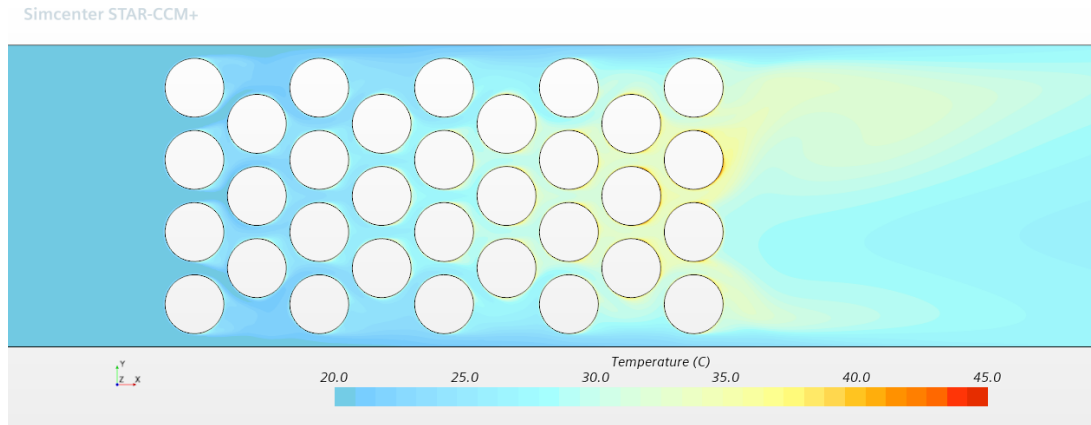


Figure 4.14: Staggered velocity scene, inlet $V = 2$ m/s

At the boundary the temperature of the cylinders is lower because of the breathing space available but at the center this arrangement of cells lead to higher temperature values due to congestion. In Figure 4.14 it is evident the air temperature around the cells for near the boundary is lower for the first three rows but majority of the heat is getting concentrated in the last 3 rows, this lead to uneven distribution of heat which severely effects the performance of the battery pack. The temperature difference within the pack for a staggered arrangement for an inlet velocity of 2 m/s is 43 % higher in comparison with aligned arrangement.

In cross arrangement, the average velocity is same as the aligned but because the cells are placed in cross the overall width of the jet-stream that is formed between the cell rows decreases, unlike the staggered arrangement there is no breathing space available in cross arrangement. This arrangement is the most compact one, and has the highest drag value. The effect of this is visible on the temperature scene.

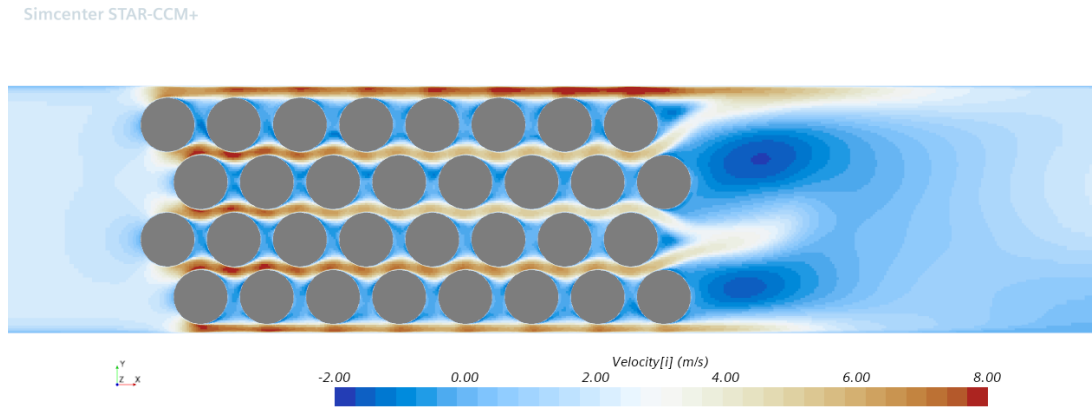


Figure 4.15: Cross velocity scene, inlet $V = 2$ m/s

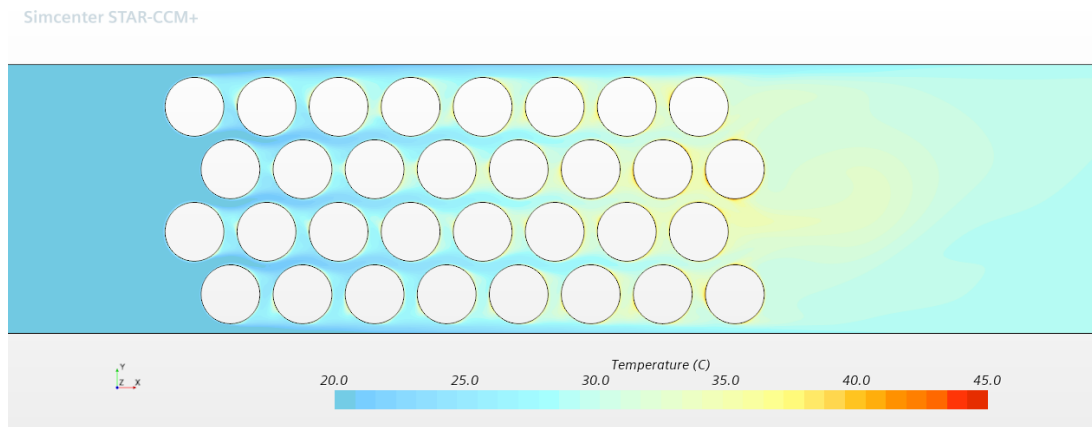


Figure 4.16: Cross velocity scene, inlet $V = 2$ m/s

The cross arrangement has the highest temperature rise among all the three configurations. Though the arrangement has the highest space utilization factor, a higher inlet velocity would be required to maintain the temperature of the pack. Which decreases the overall efficiency of the system.

CHAPTER 5: CONCLUSIONS

To study the heat transfer and thermal dissipation for 32 high energy density cylindrical lithium-ion batteries was conducted using simecenter starccm+ with a battery designed with the help of battery design studio. Battery design studio provided a platform for designing the detailed model for the lithium-ion battery while considering all the key parameters like appropriate active material, jelly roll dimensions, internal posts and tabs, separator, electrolyte, etc. which contributed towards heat generation within a battery.

During the set-up period study on the impact of velocity and pressure gradients near the outlet is studied and analyzed. A plenum in the down-stream direction and a slip box is added in the upstream extension to facilitate proper flow field development.

The simulation revealed the most appropriate turbulence model for modelling such simulations is the standard $k - \epsilon$ model, the current study involves complex recirculating, rotating, jet impinging flows which is wall bounded, $k - \epsilon$ model and its variation have been proven to capture these flows more accurately [52]. The realizable $k - \epsilon$ model was the second best model, and the SST and elliptic blending model showed high over-prediction for low velocity values. The results from the numerical simulation for discharge rate 2C and 1C are validated after comparing them with experimental results by Yuqian et. al [1]

The effect of heat generation with change in discharge rate is studied, while designing a battery thermal management system we need to keep in mind the maximum discharge rate. As the discharge rate changes from 2C to 1C the temperature values for $\Delta T_{rise,max}$ and ΔT_{max} drop around 3 times. Different inlet velocities for differ-

ent discharge rates can be used in order to increase efficiency of the battery thermal management system.

The results show full alignment with experimental results for velocities 2 m/s, 3 m/s and 4 m/s. There is over-prediction observed for inlet velocities 0.6 m/s and 1 m/s. The cause of this can be related to the inability of the turbulence models in our study to predict accurate results for natural convection simulations, secondly the effect of ambient temperature on heat generation of the battery.

The inlet velocities have a significant impact in temperature distribution, if we look at figure 4.2, we can see the impact in drop of maximum temperature rise on increasing the velocity from 0.6 m/s to 1 m/s is about 10 °C, but as we increases the velocity further more this trend of temperature reduction weakens. A battery pack should not have a temperature difference of more than 5 °C as it affects the proper functioning of the pack and can lead to over heating which can cause thermal runaway [3] . Hence the velocity for this battery pack, at 2C discharge rate should be at-least 4 m/s and 2 m/s for 1C discharge rate.

After analyzing the aligned, staggered and cross arrangement, we can say that the aligned arrangement has the best temperature uniformity and cooling effectiveness. The staggered arrangement though has maintained a lower temperature for the first three rows, there is considerable temperature rise in the last four rows, which increases the value of temperature max difference. After looking at the temperature distribution scene we can conclude that this arrangement is not the most ideal one, it has a low space utilization percentage and uneven temperature distribution. But for some reason we want to use this arrangement we need to provide extra air flow inlets/ducts for cooling the later half the pack to avoid over-heating.

The cross arrangement has the best space utilization percentage, but because of that the temperature of the whole pack increases though it is uniform compared to staggered arrangement the overall temperature is higher, we would need a higher inlet

velocity for using such a configuration to prevent over-heating. It could be used in places where we require densely packed batteries.

The difference in temperature values of aligned, cross and staggered arrangement display the effect of wake generation behind the cylinders/battery cell on the convective heat transfer coefficient. The cells themselves acts as resistance to the flow of air, and there are small wake region developed behind each cell, these wake regions act as hotspots. For aligned arrangement we reduce this resistance and hence the heat dissipation is faster and higher, for staggered arrangement we fail to provide uniform breathing spaces hence there is less temperature uniformity. Lastly for cross, the compactness and resistance by cells both are present which leads to highest temperature values.

Lastly, a numerical analysis that provides a framework for future research on aero-thermal simulation of electric vehicle using a popular commercial CFD code is conducted. This study can act as a base in conducting full body automotive aero-thermal analysis on one platform. It can also be used for studying thermal runaway in a battery pack. There is extensive work done on thermal runaway using finite element method [17], [6], this study can form a base for conducting finite volume method analysis.

REFERENCES

- [1] Y. Fan, Y. Bao, C. Ling, Y. Chu, X. Tan, and S. Yang, "Experimental study on the thermal management performance of air cooling for high energy density cylindrical lithium-ion batteries," *Applied Thermal Engineering*, vol. 155, pp. 96–109, 2019.
- [2] J. Sturm, A. Rheinfeld, I. Zilberman, F. B. Spingler, S. Kosch, F. Frie, and A. Jossen, "Modeling and simulation of inhomogeneities in a 18650 nickel-rich, silicon-graphite lithium-ion cell during fast charging," *Journal of Power Sources*, vol. 412, pp. 204–223, 2019.
- [3] D. Ouyang, J. Liu, M. Chen, J. Weng, and J. Wang, "An experimental study on the thermal failure propagation in lithium-ion battery pack," *Journal of The Electrochemical Society*, vol. 165, no. 10, p. A2184, 2018.
- [4] L. H. Saw, Y. Ye, A. A. Tay, W. T. Chong, S. H. Kuan, and M. C. Yew, "Computational fluid dynamic and thermal analysis of lithium-ion battery pack with air cooling," *Applied energy*, vol. 177, pp. 783–792, 2016.
- [5] J. Xu, L. Wang, J. Guan, and S. Yin, "Coupled effect of strain rate and solvent on dynamic mechanical behaviors of separators in lithium ion batteries," *Materials & Design*, vol. 95, pp. 319–328, 2016.
- [6] X. Feng, M. Ouyang, X. Liu, L. Lu, Y. Xia, and X. He, "Thermal runaway mechanism of lithium ion battery for electric vehicles: A review," *Energy Storage Materials*, vol. 10, pp. 246–267, 2018.
- [7] G.-H. Kim, A. Pesaran, and R. Spotnitz, "A three-dimensional thermal abuse model for lithium-ion cells," *Journal of Power Sources*, vol. 170, no. 2, pp. 476–489, 2007.
- [8] G. Zhong, H. Li, C. Wang, K. Xu, and Q. Wang, "Experimental analysis of thermal runaway propagation risk within 18650 lithium-ion battery modules," *Journal of the Electrochemical Society*, vol. 165, no. 9, p. A1925, 2018.
- [9] Z. Liao, S. Zhang, K. Li, G. Zhang, and T. G. Habetler, "A survey of methods for monitoring and detecting thermal runaway of lithium-ion batteries," *Journal of Power Sources*, vol. 436, p. 226879, 2019.
- [10] T. Wu, H. Chen, Q. Wang, and J. Sun, "Comparison analysis on the thermal runaway of lithium-ion battery under two heating modes," *Journal of hazardous materials*, vol. 344, pp. 733–741, 2018.
- [11] J. Bredberg, S. Peng, and L. Davidson, "On the wall boundary condition for computing turbulent heat transfer with k-omega models," *ASME-PUBLICATIONS-HTD*, vol. 366, pp. 243–250, 2000.

- [12] F. R. Menter, M. Kuntz, and R. Langtry, “Ten years of industrial experience with the sst turbulence model,” *Turbulence, heat and mass transfer*, vol. 4, no. 1, pp. 625–632, 2003.
- [13] Z. Yang and T.-H. Shih, “New time scale based k-epsilon model for near-wall turbulence,” *AIAA journal*, vol. 31, no. 7, pp. 1191–1198, 1993.
- [14] F. Billard and D. Laurence, “A robust k- ϵ - v^2/k elliptic blending turbulence model applied to near-wall, separated and buoyant flows,” *International Journal of Heat and Fluid Flow*, vol. 33, no. 1, pp. 45–58, 2012.
- [15] J. Liang, Y. Gan, and Y. Li, “Investigation on the thermal performance of a battery thermal management system using heat pipe under different ambient temperatures,” *Energy conversion and management*, vol. 155, pp. 1–9, 2018.
- [16] C. Zhang, S. Santhanagopalan, M. A. Sprague, and A. A. Pesaran, “Coupled mechanical-electrical-thermal modeling for short-circuit prediction in a lithium-ion cell under mechanical abuse,” *Journal of Power Sources*, vol. 290, pp. 102–113, 2015.
- [17] Y. Xia, T. Li, F. Ren, Y. Gao, and H. Wang, “Failure analysis of pinch-torsion tests as a thermal runaway risk evaluation method of li-ion cells,” *Journal of Power Sources*, vol. 265, pp. 356–362, 2014.
- [18] H. Sun, X. Wang, B. Tossan, and R. Dixon, “Three-dimensional thermal modeling of a lithium-ion battery pack,” *Journal of Power Sources*, vol. 206, pp. 349–356, 2012.
- [19] X. Li, F. He, and L. Ma, “Thermal management of cylindrical batteries investigated using wind tunnel testing and computational fluid dynamics simulation,” *Journal of power sources*, vol. 238, pp. 395–402, 2013.
- [20] S. Al Hallaj, J. Prakash, and J. Selman, “Characterization of commercial li-ion batteries using electrochemical-calorimetric measurements,” *Journal of Power Sources*, vol. 87, no. 1-2, pp. 186–194, 2000.
- [21] R. Liu, J. Chen, J. Xun, K. Jiao, and Q. Du, “Numerical investigation of thermal behaviors in lithium-ion battery stack discharge,” *Applied energy*, vol. 132, pp. 288–297, 2014.
- [22] R. Sabbah, R. Kizilel, J. Selman, and S. Al-Hallaj, “Active (air-cooled) vs. passive (phase change material) thermal management of high power lithium-ion packs: Limitation of temperature rise and uniformity of temperature distribution,” *Journal of Power Sources*, vol. 182, no. 2, pp. 630–638, 2008.
- [23] R. Zhao, J. Gu, and J. Liu, “An experimental study of heat pipe thermal management system with wet cooling method for lithium ion batteries,” *Journal of power sources*, vol. 273, pp. 1089–1097, 2015.

- [24] Z. Ling, F. Wang, X. Fang, X. Gao, and Z. Zhang, "A hybrid thermal management system for lithium ion batteries combining phase change materials with forced-air cooling," *Applied energy*, vol. 148, pp. 403–409, 2015.
- [25] S. Shahid and M. Agelin-Chaab, "Experimental and numerical studies on air cooling and temperature uniformity in a battery pack," *International Journal of Energy Research*, vol. 42, no. 6, pp. 2246–2262, 2018.
- [26] K. Chen, Y. Chen, Z. Li, F. Yuan, and S. Wang, "Design of the cell spacings of battery pack in parallel air-cooled battery thermal management system," *International Journal of Heat and Mass Transfer*, vol. 127, pp. 393–401, 2018.
- [27] R. Mahamud and C. Park, "Reciprocating air flow for li-ion battery thermal management to improve temperature uniformity," *Journal of Power Sources*, vol. 196, no. 13, pp. 5685–5696, 2011.
- [28] M. Doyle, T. F. Fuller, and J. Newman, "Modeling of galvanostatic charge and discharge of the lithium/polymer/insertion cell," *Journal of the Electrochemical society*, vol. 140, no. 6, p. 1526, 1993.
- [29] Simcenter Battery design Studio, *BDS Manual*. Siemens Digital Industries software, New York, latest ed., 2020. See also URL <https://www.plm.automation.siemens.com/global/en/products/simcenter/BDS.html>.
- [30] M. Armand, "Intercalation electrodes in" materials for advanced batteries", dw murphy, j," *Pl. Press, NY*, 1980.
- [31] H. Gu, "Mathematical analysis of a zn/niooh cell," *Journal of the Electrochemical Society*, vol. 130, no. 7, p. 1459, 1983.
- [32] U. S. Kim, C. B. Shin, and C.-S. Kim, "Modeling for the scale-up of a lithium-ion polymer battery," *Journal of Power Sources*, vol. 189, no. 1, pp. 841–846, 2009.
- [33] J. Newman and W. Tiedemann, "Potential and current distribution in electrochemical cells: Interpretation of the half-cell voltage measurements as a function of reference-electrode location," *Journal of The Electrochemical Society*, vol. 140, no. 7, p. 1961, 1993.
- [34] E. Leksono, I. N. Haq, M. Iqbal, F. N. Soelami, and I. Merthayasa, "State of charge (soc) estimation on lifepo 4 battery module using coulomb counting methods with modified peukert," in *2013 Joint International Conference on Rural Information & Communication Technology and Electric-Vehicle Technology (rICT & ICeV-T)*, pp. 1–4, IEEE, 2013.
- [35] M. Verbrugge and E. Tate, "Adaptive state of charge algorithm for nickel metal hydride batteries including hysteresis phenomena," *Journal of Power Sources*, vol. 126, no. 1-2, pp. 236–249, 2004.

- [36] S. Wang, M. Verbrugge, J. S. Wang, and P. Liu, "Power prediction from a battery state estimator that incorporates diffusion resistance," *Journal of Power Sources*, vol. 214, pp. 399–406, 2012.
- [37] W. Jones and B. E. Launder, "The prediction of laminarization with a two-equation model of turbulence," *International journal of heat and mass transfer*, vol. 15, no. 2, pp. 301–314, 1972.
- [38] B. E. Launder and B. I. Sharma, "Application of the energy-dissipation model of turbulence to the calculation of flow near a spinning disc," *Letters in heat and mass transfer*, vol. 1, no. 2, pp. 131–137, 1974.
- [39] T.-H. Shih, W. W. Liou, A. Shabbir, Z. Yang, and J. Zhu, "A new k - ϵ eddy viscosity model for high reynolds number turbulent flows," *Computers & fluids*, vol. 24, no. 3, pp. 227–238, 1995.
- [40] D. Wilcox, "A half century historical review of the k - ω model," in *29th Aerospace Sciences Meeting*, p. 615, 1991.
- [41] P. A. Durbin, "Near-wall turbulence closure modeling without damping functions," *Theoretical and computational fluid dynamics*, vol. 3, no. 1, pp. 1–13, 1991.
- [42] F. He and L. Ma, "Thermal management in hybrid power systems using cylindrical and prismatic battery cells," *Heat Transfer Engineering*, vol. 37, no. 6, pp. 581–590, 2016.
- [43] U. Rist and H. Fasel, "Direct numerical simulation of controlled transition in a flat-plate boundary layer," *Journal of Fluid Mechanics*, vol. 298, pp. 211–248, 1995.
- [44] Y. Na and P. Moin, "Direct numerical simulation of a separated turbulent boundary layer," *Journal of Fluid Mechanics*, vol. 374, pp. 379–405, 1998.
- [45] M. Sosnowski, J. Krzywanski, K. Grabowska, and R. Gnatowska, "Polyhedral meshing in numerical analysis of conjugate heat transfer," in *EPJ Web of Conferences*, vol. 180, p. 02096, EDP Sciences, 2018.
- [46] J. Córcoles-Tendero, J. Belmonte, A. Molina, and J. Almendros-Ibáñez, "Numerical simulation of the heat transfer process in a corrugated tube," *International Journal of Thermal Sciences*, vol. 126, pp. 125–136, 2018.
- [47] S. Kenjereš and K. Hanjalić, "Prediction of turbulent thermal convection in concentric and eccentric horizontal annuli," *International journal of heat and fluid flow*, vol. 16, no. 5, pp. 429–439, 1995.
- [48] T. Peeters and R. Henkes, "The reynolds-stress model of turbulence applied to the natural-convection boundary layer along a heated vertical plate," *International journal of heat and mass transfer*, vol. 35, no. 2, pp. 403–420, 1992.

- [49] S.-K. Choi and S.-O. Kim, “Turbulence modeling of natural convection in enclosures: A review,” *Journal of Mechanical Science and Technology*, vol. 26, no. 1, pp. 283–297, 2012.
- [50] Y. Xie, S. Shi, J. Tang, H. Wu, and J. Yu, “Experimental and analytical study on heat generation characteristics of a lithium-ion power battery,” *International Journal of Heat and Mass Transfer*, vol. 122, pp. 884–894, 2018.
- [51] M. Cook, Y. Ji, and G. Hunt, “Cfd modelling of natural ventilation: combined wind and buoyancy forces,” *International Journal of Ventilation*, vol. 1, no. 3, pp. 169–179, 2003.
- [52] D. Singh, B. Premachandran, and S. Kohli, “Numerical simulation of the jet impingement cooling of a circular cylinder,” *Numerical Heat Transfer, Part A: Applications*, vol. 64, no. 2, pp. 153–185, 2013.